Detecting Speed Improvement and System Stability Enhancement for DC Microgrids Islanding Detection Based on Impedance Characteristic Analysis

Tianling Shi, *Student Member, IEEE*, Hongyi Chen, Boxin Liu, Shiyuan Fan,
Fei Wang, *Senior Member, IEEE*, Xin Xiang, *Senior Member, IEEE*, Huan Yang, *Member, IEEE*,
and Wuhua Li, *Member, IEEE*

***Abstract*—Islanding detection is the essential basis for the safety and protection of dc microgrids. Due to the advantages of rapid detection speed and small nondetection zone, the positive feedback islanding detection technique has attracted much interest in recent years. The implementation of a positive feedback loop facilitates the islanding detection for dc microgrids, but it may reduce the system stability margin at the grid-connected state. In this article, the dc output impedance model of voltage source converter and distributed generators are developed to reveal the dynamic interactions and instability mechanism accurately between the two subsystems considering the impact of islanding detection with voltage positive feedback of selected frequency (VPFOSF). Then, the stability region of the interconnected system based on the output admittance model is derived to guide the design method of the damping compensator. Moreover, a grid-current-based active-damping control scheme is further proposed to mitigate instability caused by the VPFOSF loop. Thus, the conflict among islanding detection rapidity, power quality, and grid-connected system stability is effectively addressed. In the end, both the simulations and experimental results are provided to validate the effectiveness of the proposed control method.**

***Index Terms*—Active-damping control, dc microgrids, impedance-based analysis, islanding detection, stability region.**

NOMENCLATURE

p_{ref}	Power reference of DG controller.
p_{dg}	DG output power.
v_{dg}	DG PCC voltage.
C_{dg}	Equivalent bus capacitance connected at the DG PCC.
i_{ref}	Current reference of DG controller.
i_{dg}	DG output current.
i_{dis}	Current disturbance command.
$L_{\text{dc}}, R_{\text{dc}}$	Filter inductance and resistance of the dc/dc converter.
v_{dc}	DC grid voltage.
v_{ref}	DC grid voltage reference.
i_{dc}	DC grid current.
$L_{\text{ac}}, R_{\text{ac}}$	Filter inductance and resistance on the ac side of the VSC.
$i_{d\_\text{ref}}, i_{q\_\text{ref}}$	*d*-axis and *q*-axis current reference.
i_d, i_q	*d*-axis and *q*-axis grid current.
ω_g	Angular frequency of the ac grid voltage.
$L_{\text{line}}, R_{\text{line}}$	Inductance and resistance of transmission line.
R_L	Load resistance.
K_r	Positive feedback gain of the resonator.
ω_r	Resonant bandwidth.
f_0	Selected resonant frequency.
s	Laplace operator.
$\hat{}$	Small-signal disturbance.

I. INTRODUCTION

With the extensive application of dc distributed generators (DGs) and loads [1], [2], [3], such as photovoltaic, energy storage systems, electric vehicles, etc., the dc microgrid has been increasingly used due to its higher efficiency, fewer power conversion steps, and no concerns on reactive power [4], [5], [6]. Massive efforts have been taken on the techniques of power distribution, voltage regulation, and stabilizing control to enhance the dc system performance [7], [8], [9], [10]. Nonetheless, islanding detection in dc microgrids still faces challenges due to the lack of detecting freedom. In general, islanding is defined as the disconnection of the microgrid from the utility grid, where the exact power that neutralizes between DGs and loads is the worst case, namely unconscious islanding [11], [12], [13]. The failure to detect unconscious islanding may endanger the safety of both customer equipment and maintenance personnel [14], [15], making it urgent to develop a simple and practical dc islanding detection scheme (IDS).

Manuscript received 15 July 2022; revised 17 October 2022; accepted 3 November 2022. Date of publication 14 November 2022; date of current version 26 December 2022. This work was supported in part by the National Natural Science Foundation of China under Grant 51977126, in part by the National Key Research and Development Program of China under Grant 2022YFE0101900, and in part by the National Natural Science Foundation of China under Grant 52107214. Recommended for publication by Associate Editor M. Liserre. *(Corresponding authors: Fei Wang; Xin Xiang.)*

Tianling Shi and Fei Wang are with the Shanghai Key Laboratory of Power Station Automation Technology, School of Mechatronics Engineering and Automation, Shanghai University, Shanghai 200444, China (e-mail: tianlingshi@shu.edu.cn; f.wang@i.shu.edu.cn).

Hongyi Chen, Boxin Liu, Shiyuan Fan, Xin Xiang, Huan Yang, and Wuhua Li are with the College of Electrical Engineering, Zhejiang University, Hangzhou 310027, China (e-mail: hongyi.chen@zju.edu.cn; liuboxin@zju.edu.cn; shiyuan_fan@zju.edu.cn; xiangxin@zju.edu.cn; yanghuan@zju.edu.cn; woohualee@zju.edu.cn).

Color versions of one or more figures in this article are available at https://doi.org/10.1109/TPEL.2022.3221741.

Digital Object Identifier 10.1109/TPEL.2022.3221741

IDSs for dc microgrids have been intensively investigated in recent years. In [16] and [17], simple passive IDSs are proposed based on continuously measuring the change of voltage and current under power mismatching conditions, but they have large nondetection zones (NDZ) [18]. On the other hand, many active IDSs, such as impedance-measurement-based methods [18], [19], [20], [21] and positive-feedback-based methods [22], [23], [24] are proposed to detect the islanding state by adding small disturbance signals to the controller and monitoring different system responses. Among them, the positive feedback-based IDS has attracted great attention as a promising technique in dc microgrids due to its advantages of rapid detection speed and small NDZ.

Based on the positive feedback mechanism, islanding detection with square wave perturbation (SWP) method, full band positive feedback (FBPF) method, and voltage positive feedback of selected frequency (VPFOSF) method are further proposed. In [22], SWP proportional to the fluctuation of the point of common coupling (PCC) voltage was injected into the current loop of the DG controller. Under islanding conditions, the voltage fluctuation was affected by the current imbalance until its amplitude was out of the set threshold. However, the appropriate design method of the perturbation and system stability was not fully studied. To investigate the range of disturbance parameters and stability issues of positive-feedback-based dc IDS, FBPF method was proposed in [23] with the detailed feedback gain design. The perturbation proportional to the PCC voltage deviation was applied to either the power or current control loop of the DG to constitute voltage positive feedback. During islanding events, the PCC voltage gradually oscillated until it was shifted out of the allowed range. At the same time, Mohamad and Mohamed [25] and [26] developed an active-damping method to mitigate instabilities caused by the constant power loads (CPLs) and FBPF loop dynamic interactions. In this manner, fast islanding detection could be realized and the overall system stability could be also ensured. However, the FBPF scheme has an inherent disadvantage that it requires forcing the voltage out of the allowed operating range to indicate islanding events, which has negative effects on the power quality. To solve this problem, the VPFOSF islanding detection method was further proposed in [24]. It is advantageous over the above methods because islanding events can be indicated by causing the PCC voltage to oscillate with small amplitudes at a particular frequency without the necessity to shift the voltage amplitude out of the normal range. The VPFOSF IDS realized good power quality during islanding events, but its grid-connected system stability relied on the tradeoff paraments design method, which sacrifices the detection speed. More importantly, the instability mechanism of the grid-connected dc microgrid was not investigated in detail. Therefore, the conflict among islanding detection rapidity, power quality, and grid-connected system stability needs to be further amazed and addressed.

In this article, the VPFOSF method is used to detect islanding events as it can guarantee power quality and easily distinguish islanding events from other faults that may cause large voltage fluctuations. Then, the dynamic interactions and instability mechanism of the grid-connected dc microgrid are revealed accurately by developing dc output impedance models of voltage source converter (VSC) and DG considering the effect of VPFOSF IDS. With the help of the impedance-based analysis, a simple and practical active-damping method is further proposed to improve the islanding detection speed and the grid-connected system stability. The major contributions of this article can be summarized as follows:

1) Investigating and characterizing the effect of the VPFOSF paraments setting on the islanding detection speed and system stability.
2) The stability region of the grid-connected dc microgrid considering the impact of VPFOSF loop is derived, which guides the design method of a concise and valid damping compensator.
3) A grid-current-based active-damping stabilizing method is proposed to mitigate instabilities caused by the VPFOSF scheme, which effectively addresses the conflict among islanding detection rapidity, grid-connected system stability, and power quality.

The rest of this article is organized as follows. A brief description of a dc microgrid and the implementation of the VPFOSF IDS are given in Section II. The stability and dynamic interactions are analyzed based on the impedance models of the VSC and DG considering the VPFOSF effect in Section III. The design principles of the proposed active-damping stabilizing method are highlighted in Section IV. Sections V and VI demonstrate the full-scale simulation and down-scale experimental results, respectively, which both verify the theoretical analysis. Finally, the conclusions are summarized in Section VII.

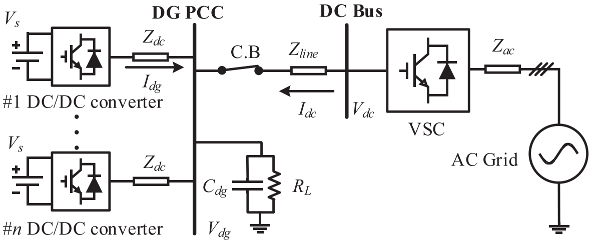

Fig. 1. Typical grid-connected dc microgrid.

II. DC MICROGRID WITH VPFOSF IDS

An introduction of a typical dc microgrid with islanding detection is presented in the following and the detailed model of DG converter is established as the foundation of VPFOSF IDS implementation. Using this model, the selection of the most sensitive disturbance frequency is presented to cause the PCC voltage most likely to oscillate during islanding events, and the impact on detection speed with feedback gain K_r and bandwidth ω_r variation is also illustrated.

A. System Description

Fig. 1 illustrates a typical dc microgrid with islanding detection, where multiple DGs are connected in a bus configuration. The DG is connected to a dc/dc converter to deliver the constant power to the load R_L [27], which is represented by a pure resistance as it has the largest NDZ [11], [23]. When the circuit

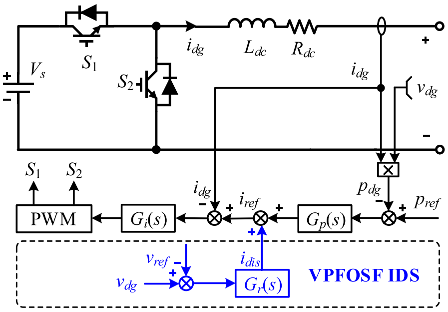

Fig. 2. Structure of the DG converter with islanding detection.

TABLE I
SIMULATION AND EXPERIMENTAL PARAMETERS OF DG

Parameters	Simulation	Experiment
Rated DG source voltage V_s	600 V	300 V
Rated DG power P_{dg}	100 kW	0.8 kW
Filter inductance L_{dg}	2 mH	2.4 mH
Switching frequency	10 kHz	10 kHz
Bus capacitance C_{dg}	2000 µF	2200 µF
Proportion gain of power controller K_{pp}	$1.2*10^{-5}$	0.005
Integral gain of power controller K_{pi}	0.75	0.5
Proportion gain of current controller K_{ip}	0.0249	0.0593
Integral gain of current controller K_{ii}	18.77	44.78

breaker is closed, the ac grid is connected to a VSC to regulate the PCC voltage [28]. Z_{ac} and Z_{dc} are the filter impedance of the VSC and DG, respectively. Z_{line} is the impedance of the transmission line, and C_{dg} is the equivalent bus capacitance connected at the DG PCC. The implementation of the VPFOSF IDS based on this system is presented in the following.

In general conditions, the DG source serves as a constant power source to develop and validate the islanding detection performance [23], [24]. As exhibited in Fig. 2, the DG controller consists of power and current double-loop control to feed constant power to the local loads, and its small-signal model is presented in Fig. 3. Both the power controller $G_p(s)$ and current controller $G_i(s)$ are PI controllers for fast and zero error tracking. The main idea of the current-loop-based VPFOSF scheme is applied by sending the PCC voltage deviation to the frequency selection $G_r(s)$ to achieve the disturbing current i_{dis}. This technique is equally valid for other types of configurations as long as the DG controller without participating in bus voltage regulation, which may conflict with the positive feedback loop and result in islanding detection failure. The principle of obtaining this disturbance with selected frequency is presented in Fig. 4. In detail, a proportional-resonant controller expressed in (1) is integrated into the positive feedback loop to form a frequency selection. Then, the dc/dc converter, including its basic control loop, is equivalent to an amplifier. In this manner, as long as the frequency selection loop and amplification loop satisfy both the amplitude and phase conditions shown in (2) and (3) [29], the sinusoidal self-excited oscillator can be formed to realize oscillating at the selected frequency f_0 ($f_0 = \omega_0/2\pi$)

$$G_r\left(s\right) = \frac{2K_r\omega_r s}{s^2 + 2\omega_r s + \omega_0^2} \tag{1}$$

$$\left|A_{\mathrm{A}}\left(f_0\right) \cdot A_{\mathrm{F}}\left(f_0\right)\right| \geq 1 \tag{2}$$

$$\varphi_{\mathrm{A}}\left(f_0\right) + \varphi_{\mathrm{F}}\left(f_0\right) = 2n\pi \tag{3}$$

where $A_{\mathrm{A}}(f_0)$ and $A_{\mathrm{F}}(f_0)$ are the amplitude of the amplifier loop and feedback loop at the selected frequency f_0, respectively. $\varphi_{\mathrm{A}}(f_0)$ and $\varphi_{\mathrm{F}}(f_0)$ are the phase of the amplifier loop and feedback loop at the selected frequency f_0, respectively.

B. Selection of the Most Sensitive Disturbance Frequency

The worst condition for islanding detection is when the power of generation exactly neutralizes the power consumption. In this case, P_0 is equal to the reference power, V_0 and I_0 are the steady-state voltage and current determined by loads, respectively. To realize fast islanding detection even in the worst case when using the VPFOSF IDS, it is necessary to select the most sensitive disturbance frequency. The current balance equation of the DG unit under the islanding condition with power neutralization is linearized at the steady-state point (V_0, I_0, P_0) as follows:

$$\hat{p}_{\mathrm{dg}} = I_0\hat{v}_{\mathrm{dg}} + V_0\hat{i}_{\mathrm{dg}} \tag{4}$$

$$\hat{i}_{\mathrm{dg}} = \hat{v}_{\mathrm{dg}}\left(1/R_L + sC_{\mathrm{dg}}\right) = \hat{v}_{\mathrm{dg}}Y_{\mathrm{RC}}. \tag{5}$$

Then, according to Fig. 3, the dynamics of the current loop without VPFOSF is described as follows, where K_{PWM1} is the equivalent gain of the pulsewidth modulator (PWM):

$$\hat{i}_{\mathrm{ref}} = G_p(s)(\hat{p}_{\mathrm{ref}} - \hat{p}_{\mathrm{dg}}) \tag{6}$$

$$\hat{i}_{\mathrm{dg}} = \left[K_{\mathrm{PWM1}}G_i(s)(\hat{i}_{\mathrm{ref}} - \hat{i}_{\mathrm{dg}}) - \hat{v}_{\mathrm{dg}}\right]\Big/(R_{\mathrm{dc}} + sL_{\mathrm{dc}}). \tag{7}$$

When the VPFOSF IDS is employed, the small-signal model of the current reference given in (6) is rewritten as

$$\hat{i}_{\mathrm{ref}} = G_p(s)(\hat{p}_{\mathrm{ref}} - \hat{p}_{\mathrm{dg}}) + \hat{i}_{\mathrm{dis}}. \tag{8}$$

Setting the variation of the power reference to zero, solving (4), (5), (7), and (8), the transfer function $S_i(s)$ of the PCC voltage to the disturbing current at islanding state can be derived as follows:

$$S_i\left(s\right) = \frac{\hat{v}_{\mathrm{dg}}}{\hat{i}_{\mathrm{dis}}} = \frac{1}{G_\varphi(s) + G_\tau(s)Y_{\mathrm{RC}}} \tag{9}$$

where

$$G_\varphi(s) = I_0G_p(s) + 1/K_{\mathrm{PWM1}}G_i(s) \tag{10}$$

$$G_\tau(s) = 1 + V_0G_p(s) + (R_{\mathrm{dc}} + sL_{\mathrm{dc}})/K_{\mathrm{PWM1}}G_i(s). \tag{11}$$

To verify the correctness of (9), a frequency sweep is carried out to measure the frequency response of the PCC voltage to the disturbing current based on the MATLAB/Simulink model. The simulation parameters of a typical 100 kW, 500 V dc system are shown in Table I. Also, the theoretical frequency response curve is depicted in Fig. 5.

It clearly shows that the theoretical curve is consistent with the measured one, proving the correctness of (9). Moreover, Fig. 5 indicates that the magnitude is maximum at 60 Hz, which means that disturbing current with this frequency is the easiest choice to

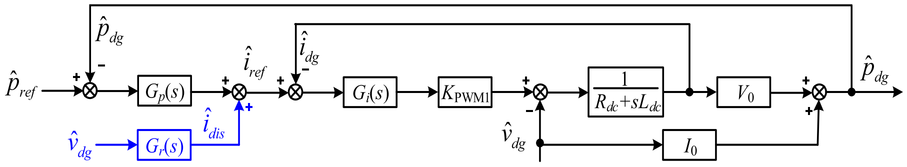

Fig. 3. Small-signal model of the DG controller.

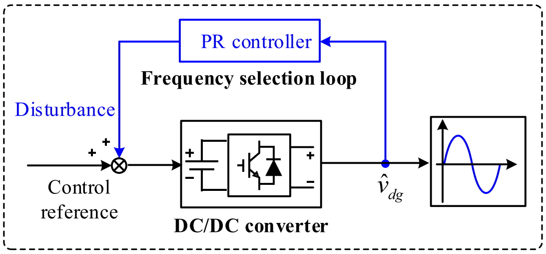

Fig. 4. Principle of the VPFOSF.

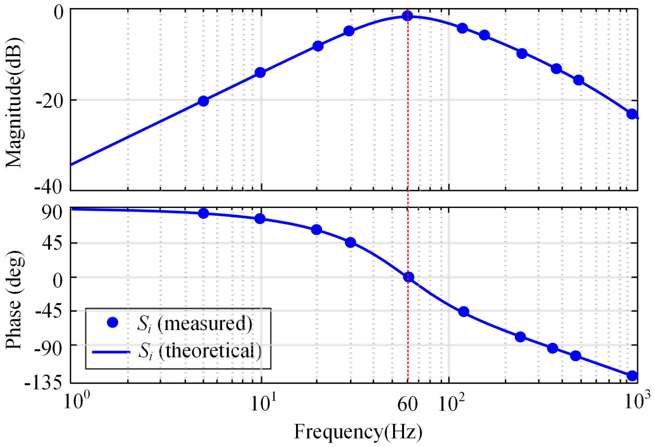

Fig. 5. Theoretical and measured frequency response of the PCC voltage to the disturbing current.

cause the PCC voltage oscillation under islanding conditions. In this manner, 60 Hz is selected as the most sensitive disturbance frequency in this article.

C. Impact on Detection Speed With K_r and ω_r Variation

According to Fig. 2, the characteristic equation of an islanding system is obtained as follows:

$$1 - G_r(s) \cdot S_i(s) = 0. \tag{12}$$

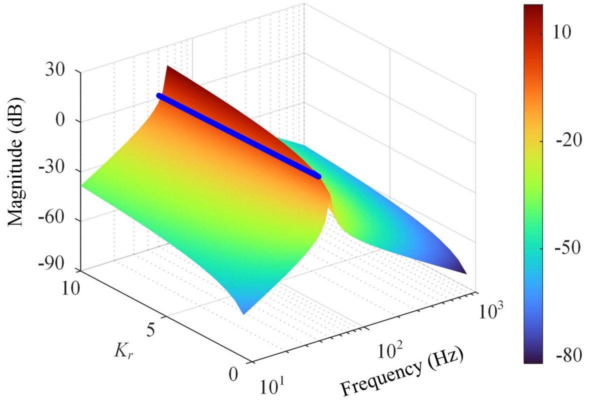

Fig. 6. Bandwidth variation of the loop gain in the islanding mode by changing K_r.

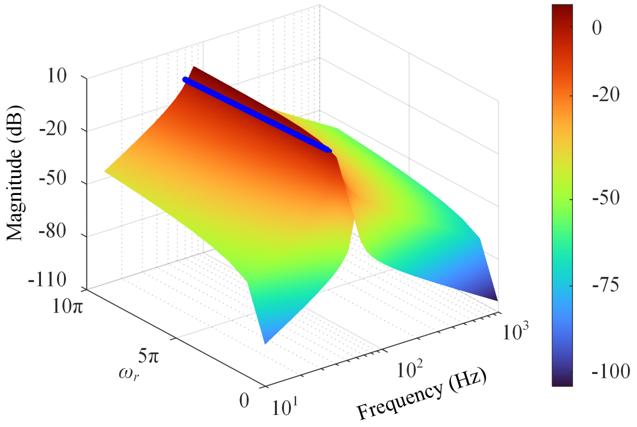

Fig. 7. Bandwidth variation of the loop gain in the islanding mode by changing ω_r.

Figs. 6 and 7 show the magnitude variation of the loop gain in the positive feedback loop at the islanding state by changing K_r and ω_r, where the blue line represents the magnitude boundary of 0 dB. It shows that the bandwidth of the loop gain above 0 dB becomes larger with the increase of K_r and ω_r, which indicates that the islanding detection speed will be further improved. By comparing Figs. 6 and 7, the variation in K_r has more significant impact on the islanding detection speed than that in ω_r. However, the rise of K_r and ω_r increases current disturbance component, which has potentially negative impacts on the grid-connected system stability. This stability issue was not investigated before [24] as it fully neglected the impedance of VSC. The dynamic interactions of the VSC and DG considering the impact of VPFOSF loop will be comprehensively analyzed by impedance-based approach in the following section to reveal the instability mechanism. Then, the stability enhancement method will be further proposed to simultaneously guarantee rapid islanding detection and overall system stability.

III. IMPEDANCE-BASED STABILITY ANALYSIS

The impedance-based method has been proved effectively in analyzing the dynamic interactions of multiconverters [30], [31],

[32], [33]. Thus, the impedance models of different converters are deduced in the following parts. Using the impedance model, the conflict between islanding detection speed and grid-connected system stability is fully illustrated. It is worth noting that in order to focus on the main work of revealing the destabilizing effect of VPFOSF loop, the detailed analysis of dc source impedance on the system stability is not included here but the relevant investigation can be readily found in recent research results [34], [35], [36].

A. DG Output Impedance Model

According to the small-signal model of the DG controller given in Fig. 3, the DG output impedance without the VPFOSF scheme is derived by

$$Z_{\mathrm{dg}}\left(s\right)=-\frac{\hat{v}_{\mathrm{dg}}}{\hat{i}_{\mathrm{dg}}}=\frac{G_{\tau}(s)}{G_{\varphi}(s)}. \tag{13}$$

When the VPFOSF scheme is employed, the dynamics of disturbing current reference given in (8) is written as

$$\hat{i}_{\mathrm{ref}}=G_p(s)(\hat{p}_{\mathrm{ref}}-\hat{p}_{\mathrm{dg}})+G_r\left(s\right)\hat{v}_{\mathrm{dg}}. \tag{14}$$

Solving (4), (7), (10), (11), and (14), the DG injected current considering VPFOSF IDS is given as follows, which illustrates the coupling between VPFOSF loop and the DG injected current dynamics:

$$\hat{i}_{\mathrm{dg}}=-\frac{G_{\varphi}(s)}{G_{\tau}(s)}\hat{v}_{\mathrm{dg}}+\frac{G_r\left(s\right)}{G_{\tau}(s)}\hat{v}_{\mathrm{dg}}. \tag{15}$$

Reformulating (15), the equivalent output admittance $Y_c(s)$ is equal to the sum of the DG intrinsic output admittance $Y_{\mathrm{dg}}(s)$ and the VPFOSF admittance $Y_{\mathrm{dis}}(s)$ as follows:

$$Y_c\left(s\right)=-\frac{\hat{i}_{\mathrm{dg}}}{\hat{v}_{\mathrm{dg}}}=Y_{\mathrm{dg}}\left(s\right)+Y_{\mathrm{dis}}\left(s\right) \tag{16}$$

where

$$Y_{\mathrm{dg}}\left(s\right)=G_{\varphi}(s)/G_{\tau}(s) \tag{17}$$

$$Y_{\mathrm{dis}}\left(s\right)=-G_r\left(s\right)/G_{\tau}(s). \tag{18}$$

Fig. 8 describes the theoretical DG output impedance Bode diagram with/without the VPFOSF scheme using the simulation parameters of the DG unit in Table I. Also, a frequency sweep is carried out to verify the accuracy of the established output impedance model. Fig. 8 shows the theoretical output impedance model matches the measured one very well. Moreover, it is obvious that the equivalent impedance Z_c with VPFOSF exhibits the same characteristics as Z_{dg} below the resonant frequency, while the magnitude and phase of Z_c are consistent with the VPFOSF impedance Z_{dis} around the selected frequency. It is evident that the VPFOSF impedance makes the equivalent impedance quickly crosses 180° to $-180°$ at oscillation frequency, which indicates the destabilizing effect of the VPFOSF loop.

B. VSC Output Impedance Model

The dynamics of the VSC and ac grid can be accurately evaluated based on the $d-q$ reference frame. Fig. 9 shows the VSC control structure, where voltage controller $G_v(s)$ and current controller $G_c(s)$ are both the PI controllers.

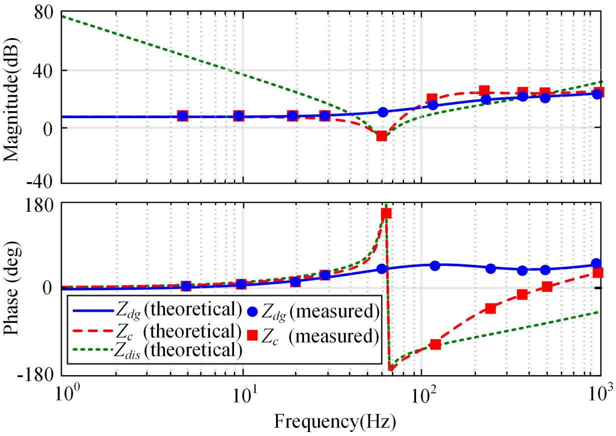

Fig. 8. Theoretical and measured impedance Bode diagram of the DG.

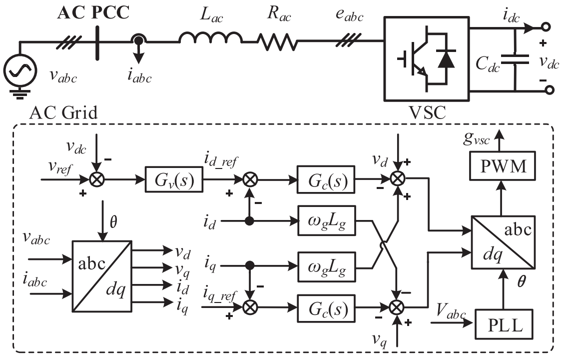

Fig. 9. Controller block diagram of the VSC.

As shown in Fig. 9, the VSC is mathematically described as

$$\begin{cases}v_d=\left(R_{\mathrm{ac}}+sL_{ac}\right)i_d-\omega_g L_{ac}i_q+e_d\\ v_q=\left(R_{\mathrm{ac}}+sL_{ac}\right)i_q+\omega_g L_{ac}i_d+e_q\end{cases} \tag{19}$$

where L_{ac} and R_{ac} are the filter inductance and parasitic resistance of the VSC, respectively. v_d and v_q are the d-axis and q-axis components of the ac grid voltage v_{abc}, respectively, e_d, and e_q are the d-axis and q-axis components of the VSC input voltage e_{abc}, respectively, and ω_g is the angular frequency of ac grid voltage.

To decouple the d-axis and q-axis variables in (19), the current feed-forward control is used in the VSC controller, and hence, e_d and e_q can be derived as follows:

$$\begin{cases}e_d=-G_c(s)(i_{d\_\mathrm{ref}}-i_d)+\omega_g L_{\mathrm{ac}}i_q+v_d\\ e_q=-G_c(s)(i_{q\_\mathrm{ref}}-i_q)-\omega_g L_{\mathrm{ac}}i_d+v_q.\end{cases} \tag{20}$$

Inserting (20) into (19), the current dynamics in d-axis and q-axis are established at the steady state (V_{dq}, I_{dq}, V_{dc}, I_{dc}) as follows:

$$\begin{cases}\hat{i}_d=G_c(s)(\hat{i}_{d\_\mathrm{ref}}-\hat{i}_d)\Big/(R_{\mathrm{ac}}+sL_{\mathrm{ac}})\\ \hat{i}_q=G_c(s)(\hat{i}_{q\_\mathrm{ref}}-\hat{i}_q)\Big/(R_{\mathrm{ac}}+sL_{\mathrm{ac}}).\end{cases} \tag{21}$$

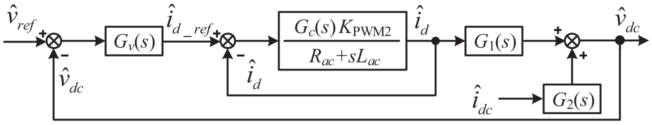

Fig. 10. Small-signal model for closed-loop control of the d-axis current.

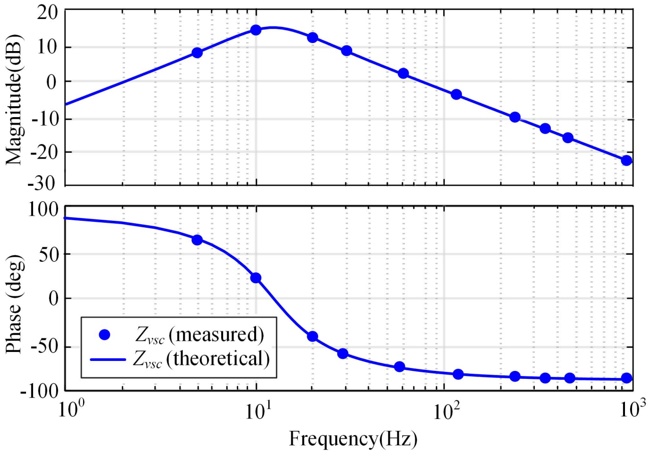

Fig. 11. Theoretical and measured impedance Bode diagram of the VSC.

Since the symmetry of the $d-q$ reference frame, the d-axis current loop is chosen for further analysis, as shown in Fig. 10. The closed-loop transfer function of the d-axis current can be derived as

$$G_d(s)=\frac{\hat{i}_d}{\hat{i}_{d\_\mathrm{ref}}}=\frac{G_c(s)K_{\mathrm{PWM2}}}{R_{\mathrm{ac}}+sL_{\mathrm{ac}}+G_c(s)K_{\mathrm{PWM2}}}\tag{22}$$

where K_{PWM2} is the equivalent gain of the PWM.

Then, according to the power balance principle between ac-side and dc-side, and setting $V_q=0$ and $I_q=0$, the small-signal model of power balance equation is given by

$$1.5\left(V_d\hat{i}_d+I_d\hat{v}_d\right)=\mathrm{s}C_{\mathrm{dc}}V_{\mathrm{dc}}\hat{v}_{\mathrm{dc}}+V_{\mathrm{dc}}\hat{i}_{\mathrm{dc}}+I_{\mathrm{dc}}\hat{v}_{\mathrm{dc}}.\tag{23}$$

Neglecting the ac grid perturbations in (23), the dynamics of the dc grid voltage is obtained as follows:

$$\hat{v}_{\mathrm{dc}}=G_1(s)\hat{i}_d+G_2(s)\hat{i}_{\mathrm{dc}}\tag{24}$$

where

$$\begin{cases}G_1(s)=\frac{\hat{v}_{\mathrm{dc}}}{\hat{i}_d}=\frac{3V_d}{2(s C_{\mathrm{dc}}V_{\mathrm{dc}}+I_{\mathrm{dc}})}\\G_2(s)=\frac{\hat{v}_{\mathrm{dc}}}{\hat{i}_{\mathrm{dc}}}=-\frac{V_{\mathrm{dc}}}{s C_{\mathrm{dc}}V_{\mathrm{dc}}+I_{\mathrm{dc}}}.\end{cases}\tag{25}$$

Thus, according to Fig. 10, the VSC output impedance model is derived as follows:

$$Z_{\mathrm{vsc}}(s)=-\frac{\hat{v}_{\mathrm{dc}}}{\hat{i}_{\mathrm{dc}}}=\frac{-G_2(s)}{1+G_v(s)G_d(s)G_1(s)}\tag{26}$$

Similarly, a frequency sweep of the dc output impedance of the VSC is carried out, as presented in Fig. 11. Obviously, it matches the theoretical impedance model very well, which demonstrates the accuracy of the developed model.

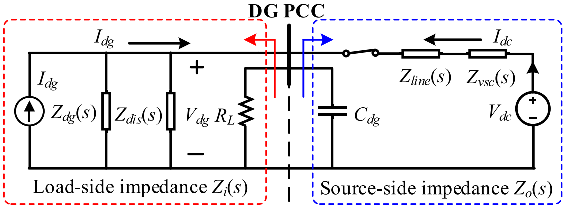

Fig. 12. Equivalent impedance circuit for the grid-connected operation.

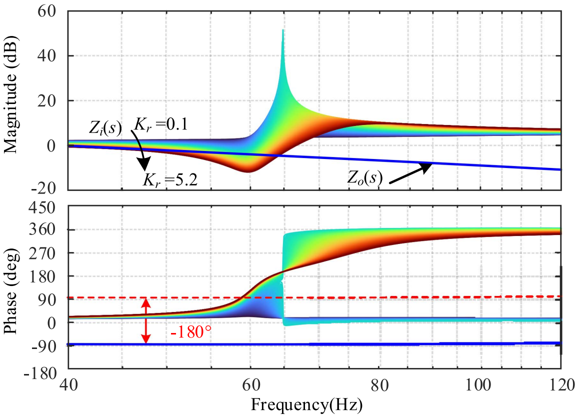

Fig. 13. Bode diagram of $Y_i(s)$ with different values of K_r.

C. Stability Analysis of Grid-Connected Operation

To analyze the grid-connected system stability with the impedance stability criteria, the equivalent impedance circuit for the grid-connected operation is developed in Fig. 12. The source-side equivalent impedance $Z_o(s)$ consists of the equivalent bus capacitance C_{dg}, the distribution feeder impedance $Z_{\mathrm{line}}(s)$, and the dc output impedance of the VSC $Z_{\mathrm{vsc}}(s)$. The load-side equivalent impedance $Z_i(s)$ includes DG output impedance $Z_{\mathrm{dg}}(s)$, VPFOSF impedance $Z_{\mathrm{dis}}(s)$, and the resistance load R_L. $Z_o(s)$ and $Z_i(s)$ are described as follows:

$$Z_o(s)=\frac{Z_{\mathrm{vsc}}(s)+Z_{\mathrm{line}}(s)}{sC_{\mathrm{dg}}\left[Z_{\mathrm{vsc}}(s)+Z_{\mathrm{line}}(s)\right]+1}\tag{27}$$

$$Z_i(s)=\frac{Z_{\mathrm{dg}}(s)Z_{\mathrm{dis}}(s)R_{\mathrm{L}}}{Z_{\mathrm{dis}}(s)R_{\mathrm{L}}+Z_{\mathrm{dg}}(s)R_{\mathrm{L}}+Z_{\mathrm{dg}}(s)Z_{\mathrm{dis}}(s)}.\tag{28}$$

In Fig. 12, the PCC voltage can be derived as (29), where $T(s)=Z_o(s)/Z_i(s)$ is the equivalent loop gain, determining the interconnected system stability. According to the impedance stability criteria, the interconnected system will be unstable if the phase difference between $Z_o(s)$ and $Z_i(s)$ exceeds $-180°$ when $|Z_o(s)|=|Z_i(s)|$. Therefore, the impact of the VPFOSF scheme on the grid-connected system stability is discussed with the help of $T(s)$ in the following:

$$V_{\mathrm{dg}}=\frac{V_{\mathrm{dc}}+I_{\mathrm{dg}}Z_o(s)}{1+Z_o(s)/Z_i(s)}=\frac{V_{\mathrm{dc}}+I_{\mathrm{dg}}Z_o(s)}{1+T(s)}.\tag{29}$$

Fig. 13 shows the amplitude and phase of load-side impedance $Z_i(s)$ with the feedback gain K_r increasing from 0.1 to 5.2 when

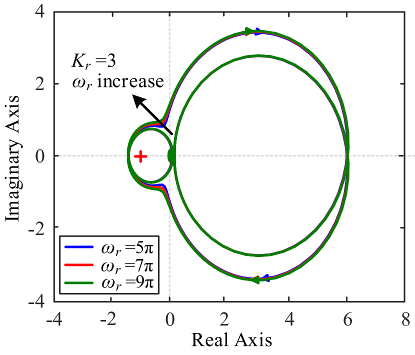

Fig. 14. Effects of ω_r variation on system stability.

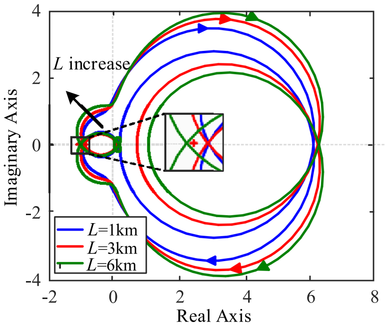

Fig. 15. Effects of transmission line lengths L variation on system stability.

ω_r and f_0 are set to 5π and 60 Hz. Obviously, with the rise of K_r, the frequency of the intersection of the curves $Z_o(s)$ and $Z_i(s)$ continues to increase, and the phase of $Z_i(s)$ gradually crosses 90° around the oscillation frequency. Since the phase of $Z_o(s)$ is close to $-90°$, the phase of $T(s)$ at the oscillation frequency would exceed $-180°$. In this case, according to the impedance stability criterion, the system will be unstable as long as $|T(s)| > 0$ dB. This means the increase of K_r can improve the islanding detection speed, but decrease stability margin of the interconnected system.

As shown in Fig. 14, the effect of increasing ω_r on the grid-connected system stability margin is investigated by the Nyquist plots of $T(s)$. It shows that although increasing ω_r slightly enhances the islanding detection speed illustrated in Fig. 7, it has less effect on the stability margin in the grid-connected mode. Thus, the root cause of the instability problem in Fig. 14 is that the selection of K_r causes the phase deviation between $Z_o(s)$ and $Z_i(s)$ around the oscillation frequency more than $-180°$.

Moreover, Fig. 15 shows the Nyquist diagrams of $T(s)$ with different transmission line lengths L under the condition of $K_r = 2$. As illustrated in Table II, the resistance and inductance of dc transmission line are 0.22 Ω/km and 0.3 mH/km, respectively. As shown in Fig. 15, with the increase of L, the Nyquist curve of $T(s)$ expands to the left half-plane, gradually enclosing $(-1, 0)$ and driving the system to an unstable state. That is because the amplitude intersection of $Z_o(s)$ and $Z_i(s)$ moves toward a higher frequency bandwidth, causing the phase deviation between them would exceed $-180°$.

TABLE II
SIMULATION AND EXPERIMENTAL PARAMETERS OF VSC AND DC GRID

Parameters	Simulation	Experiment
Rated voltage of dc grid V_{dc}	500 V	200 V
Resistance of transmission line R_{line}	0.22 Ω/km	0
Inductance of transmission line L_{line}	0.3 mH/km	0
Rated load resistance R_L	2.5 Ω	50 Ω
AC grid line voltage	190 V	105 V
VSC filter inductance L_{vsc}	2.4 mH	2.4 mH
Switching frequency	10 kHz	10 kHz
DC-link smoothing capacitor C_{dc}	2000 μF	1880 μF
Proportion gain of voltage controller K_{vp}	0.3	0.9
Integral gain of voltage controller K_{vi}	25	66
Proportion gain of current controller K_{cp}	5	5
Integral gain of current controller K_{ci}	30	3

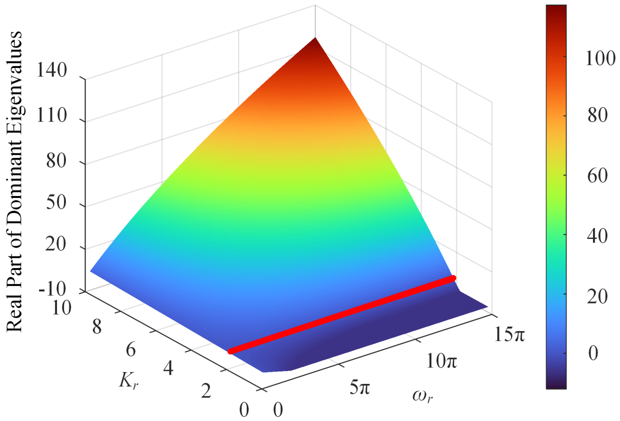

Fig. 16. Real part of dominant eigenvalues with different K_r and ω_r of grid-connected system.

Selecting the transmission line length to be 1 km, and then the conflict between islanding detection speed and grid-connected system stability can be further analyzed by dominant eigenvalues. Under grid-connected conditions, (5) can be modified as

$$\hat{i}_{\mathrm{dg}} + \hat{i}_{\mathrm{dc}} = \hat{v}_{\mathrm{dg}} Y_{RC}. \tag{30}$$

As presented in Fig. 12, the dc grid current dynamics is described as

$$\hat{i}_{\mathrm{dc}} = -\hat{v}_{\mathrm{dg}} / (Z_{\mathrm{vsc}} + Z_{\mathrm{line}}) = -Y_g \hat{v}_{\mathrm{dg}}. \tag{31}$$

Combing (4)–(8), (30), and (31), the transfer function of the PCC voltage to disturbing current at grid-connected state can be obtained as

$$S_c(s) = \frac{\hat{v}_{\mathrm{dg}}}{\hat{i}_{\mathrm{dis}}} = \frac{1}{G_\varphi(s) + G_\tau(s)\,(Y_{RC} + Y_g)}. \tag{32}$$

According to the control diagram presented in Fig. 2, the characteristic equation of the grid-connected system is expressed as

$$1 - G_r(s) \cdot S_c(s) = 0. \tag{33}$$

Setting f_0 to 60 Hz, and then the real part of dominant eigenvalues calculated by(33) in the grid-connected mode with different feedback gain K_r and bandwidth ω_r is displayed in Fig. 16. The red line represents the stability boundary in the gird-connected

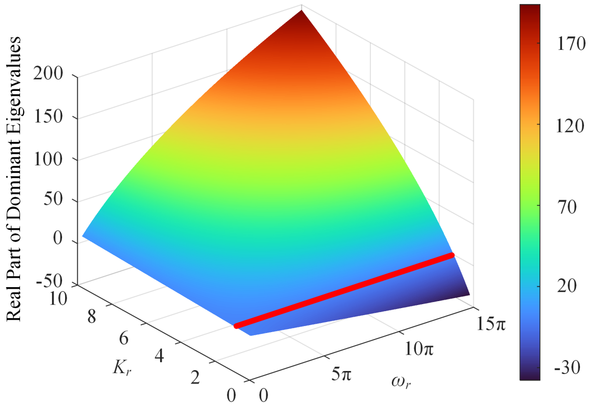

Fig. 17. Real part of dominant eigenvalues with different K_r and ω_r of islanding system.

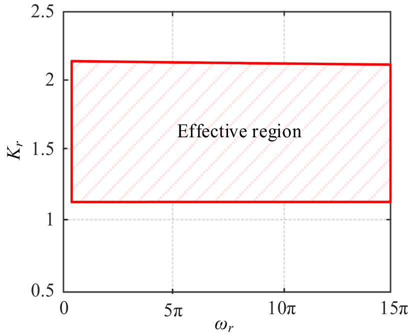

Fig. 18. Effective sets to realize rapid islanding detection while guaranteeing the grid-connected system stability.

mode, and the cases below this line mean that the overall system can preserve stability. Meanwhile, to achieve successful islanding detection, the dominant eigenvalues of islanding system need to have positive real part. As shown in Fig. 17, it shows that the real parts calculated by (12) rise rapidly with the K_r and ω_r increasing, which means that the detection speed will improve. The cases above the red line in Fig. 17 indicate that the PCC voltage is able to oscillate with the selected frequency to detect islanding events.

According to Figs. 16 and 17, the combinations of K_r and ω_r that make the dc microgrid realize rapid islanding detection while guaranteeing grid-connected system stability are described in the shadow region of Fig. 18, namely effective region. As seen from the figure, with the increase of K_r, it will exceed the effective region, indicating the instability of PCC voltage. As a result, there is always a maximum value for K_r, which sometimes can be quite small. In this situation, the system fails to keep stable even under grid-connected conditions due to the conflict between islanding detection speed and system stability. Therefore, to realize rapid islanding detection and grid-connected system stability simultaneously, a simple and practical compensating method is further presented in the following.

IV. STABILITY-REGION-BASED ACTIVE-DAMPING DESIGN

In this section, the concept of active damping is proposed to mitigate instability caused by the VPFOSF loop. Then, the stability region of the interconnected system is derived using output admittance model, which guides the design method of the proposed grid-current-based active-damping control and provides an effective solution to the conflict between islanding detection speed and grid-connected system stability.

A. Active-Damping Stabilizing

According to the previous analysis, the root cause of instability issues of the interconnected system is the VPFOSF loop causes the phase deviation between $Z_o(s)$ and $Z_i(s)$ to exceed $-180°$ around the oscillation frequency. To address this issue, an active-damping stabilizing scheme is further proposed to suppress the phase advance of $Z_i(s)$ at the actual oscillation frequency. The implementation diagram is depicted in Fig. 19, where the $G_s(s)$ is the designed active-damping stabilizing controller.

Several traditional stabilizing schemes selected the bus voltage as the feedback signal [37], [38]. They are different with the VPFOSF IDS because their stabilizer operates to stabilize the voltage, but the VPFOSF loop operates to destabilize the voltage. To avoid the malfunction of the VPFOSF IDS, the proposed active-damping stabilizing method is designed based on the dc grid current signal because the grid current will diminish in the islanding mode. In this manner, the proposed stabilizing method is only enabled under grid-connected conditions. Moreover, the stabilizing loop can suppress the phase advance issue caused by the increase of the positive feedback gain so that the detection speed and stability margin can be improved simultaneously. Therefore, the proposed active-damping stabilizing method is advantageous over these previously stabilizing schemes.

As presented in Fig. 19, the stabilizing current i_v can be obtained as

$$\hat{i}_v = G_s(s)\,\hat{i}_{\text{dc}}. \tag{34}$$

Accordingly, the DG current reference dynamics given in (14) is modified to include the active-damping loop as

$$\hat{i}_{\text{ref}} = G_p(s)(\hat{p}_{\text{ref}} - \hat{p}_{\text{dg}}) + G_r(s)\,\hat{v}_{\text{dg}} + G_s(s)\,\hat{i}_{\text{dc}}. \tag{35}$$

Solving (4), (7), (10), (11), and (35), the DG injected current dynamics is then derived as follows:

$$\hat{i}_{\text{dg}} = -\frac{G_\varphi(s)}{G_\tau(s)}\hat{v}_{\text{dg}} + \frac{G_r(s)}{G_\tau(s)}\hat{v}_{\text{dg}} - \frac{G_s(s)Y_g}{G_\tau(s)}\hat{v}_{\text{dg}}. \tag{36}$$

Reformulating (36), the update total output admittance $Y_c(s)$ can be obtained that equals the sum of the DG output admittance $Y_{dg}(s)$, the VPFOSF admittance $Y_{\text{dis}}(s)$, and the active-damping loop admittance $Y_s(s)$ as follows:

$$Y_c(s) = -\frac{\hat{i}_{\text{dg}}}{\hat{v}_{\text{dg}}} = Y_{\text{dg}}(s) + Y_{\text{dis}}(s) + Y_s(s) \tag{37}$$

where

$$Y_s(s) = 1/Z_s(s) = G_s(s)Y_g(s)/G_\tau(s). \tag{38}$$

Accordingly, the impedance model for the grid-connected dc microgrid is reshaped as Fig. 20, and thus, the equivalent loop

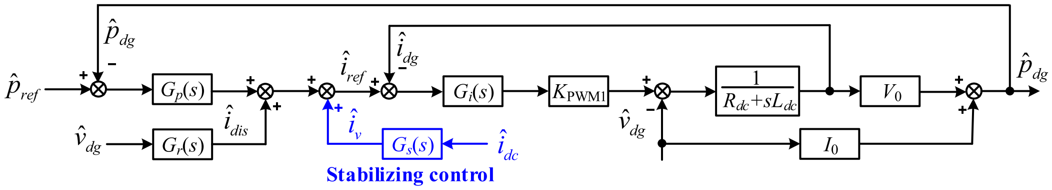

Fig. 19. Small-signal model of the DG controller with the proposed active-damping control.

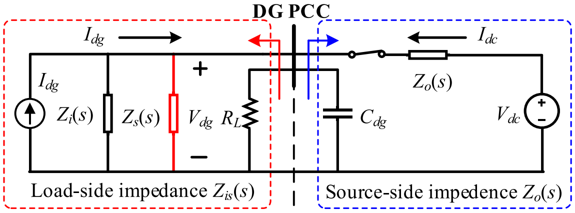

Fig. 20. Reshaped impedance model for the grid-connected dc microgrid.

gain $T(s)$ is modified as

$$T(s) = Z_o(s)\left[Y_i(s) + Y_s(s)\right] = Z_o(s) Y_{is}(s). \tag{39}$$

B. Stability Region

As described in Fig. 13, the phase of source-side impedance $Z_o(s)$ is between $-90°$ and $0°$. In this case, the interconnected system will remain stable as long as the phase of $T(s)$ stays within $[-180°, 180°]$. In light of (39), $T(s)$ is composed of $Z_o(s)$ and $Y_{is}(s)$, and their phase relationship is given by (40). Thus, to ensure that the phase range for $T(j\omega)$ satisfies the stability requirements, the allowed $\angle Y_{is}(j\omega)$ is within $[-90°, 180°]$

$$T(j\omega) = \angle Z_o(j\omega) + \angle Y_{is}(j\omega). \tag{40}$$

According to (39), the reshaped load-side admittance $Y_{is}(s)$ is decomposed into two parts: $Y_i(s)$ and $Y_s(s)$. Fig. 13 shows that the phase of $Z_i(s)$ in the instability region is between 90° and 360°. That is to say, the unstable phase range of $Y_i(s)$ is $[-360°, -90°]$. To derive the limitation of $Y_s(j\omega)$ phase, phase range of $Y_i(s)$ is divided into three parts in the following. First of all, when $\angle Y_i(j\omega)$ locating in $[-360°, -270°]$, as long as ensuring $Y_s(j\omega)$ is not in the third quadrant, $Y_{is}(j\omega)$ will never enter the forbidden region, as depicted in Fig. 21(a). Similarly, when $\angle Y_i(j\omega)$ locating in $[-270°, -180°]$, the phase range for $Y_s(j\omega)$ should be $[\angle Y_i(j\omega)+180°, 180°]$, as depicted in Fig. 21(b). Otherwise, $Y_{is}(j\omega)$ will easily enter the forbidden region as long as the $Y_s(j\omega)$ has a large magnitude. Finally, the worst condition is when $Y_i(j\omega)$ locating in $[-180°, -90°]$, as illustrated in Fig. 21(c). To ensure $\angle Y_{is}(j\omega)$ locating in the desired range, it is necessary to simultaneously ensure that the phase range for $Y_s(j\omega)$ is $[-\angle Y_i(j\omega) - 180°, -\angle Y_i(j\omega)]$, and the amplitude of $Y_s(j\omega)$ is larger than the oscillation peak of $Y_i(j\omega)$.

Based on the above analysis, the limitation of $Y_s(j\omega)$ phase and magnitude can form the stability region, as depicted in Fig. 22, where the phase of $Y_i(j\omega)$ at f_1, f_2, and f_3 is $-90°$, $-180°$, and $-270°$, respectively. That is to say, to achieve the interconnected system stability, the $Y_s(j\omega)$ should be located in the shadow region. Thus, the derived stability region provides simple and practical guide to the design method of the proposed active-damping stabilizing control method.

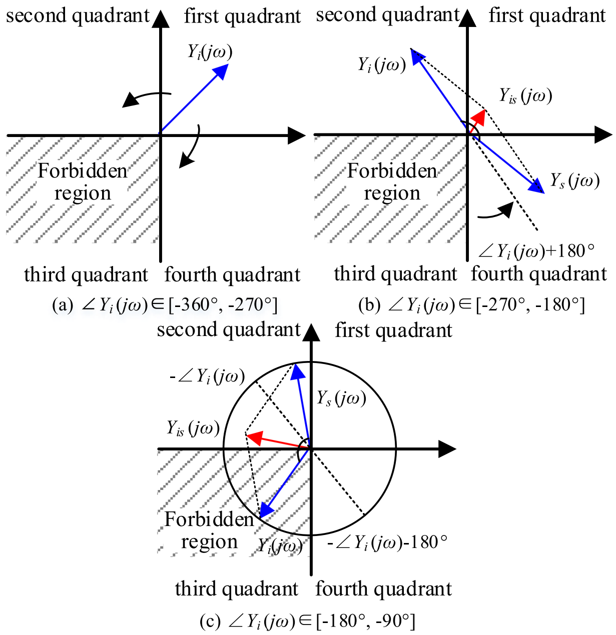

(a) $\angle Y_i(j\omega) \in [-360°, -270°]$ (b) $\angle Y_i(j\omega) \in [-270°, -180°]$

(c) $\angle Y_i(j\omega) \in [-180°, -90°]$

Fig. 21. Phasor diagram of $Y_{is}(j\omega)$.

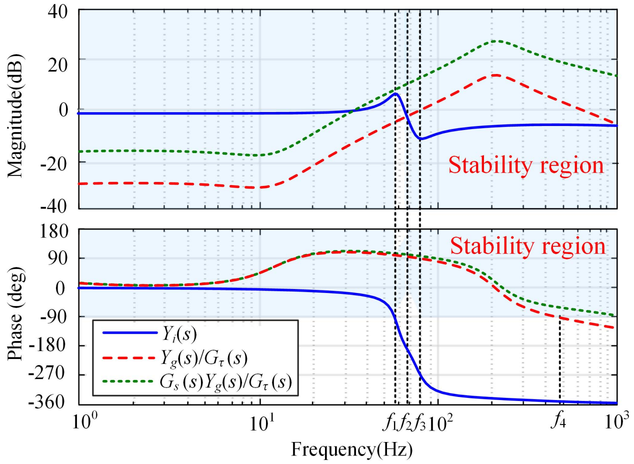

Fig. 22. Bode plots of $Y_s(s)$ with and without $G_s(s)$.

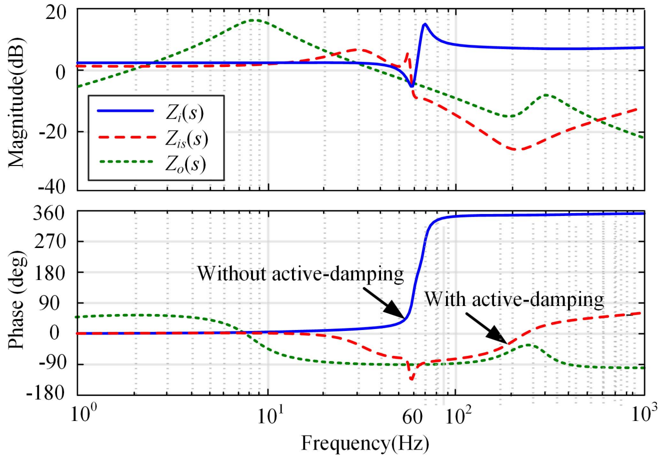

Fig. 23. Control performance of the active-damping stabilizing control.

C. Design Principles

According to (38), $Y_s(s)$ is composed of $G_s(s)$ and $Y_g(s)/G_\tau(s)$, and the bode plot of $Y_g(s)/G_\tau(s)$ is presented in Fig. 22. It is worth noting that the phase of $Y_g(s)/G_\tau(s)$ has been located in the stability region in the range of $[0, f_4]$, but it gradually turns into a negative damping characteristic at the high-frequency bandwidth. Meanwhile, the magnitude of $Y_g(s)/G_\tau(s)$ is lower than the oscillation peak in the range of $[f_1, f_2]$, which results in not being covered by the magnitude stability region. To solve this problem, the stabilizer transfer function $G_s(s)$ is presented to advance the phase of $Y_g(s)/G_\tau(s)$ at a high-frequency bandwidth by differential terms and rise its magnitude in the range of $[f_1, f_2]$ by gain terms. Furthermore, a low-pass filter is introduced to effectively avoid the harmonic amplification caused by the differentiator. Thus, the active-damping stabilizer transfer function $G_s(s)$ can be obtained as follows:

$$G_s(s) = K_s \frac{s+\omega_4}{s+\omega_c} \tag{41}$$

where $\omega_4 = 2\pi f_4$, K_s is the stabilizing gain, and ω_c is the cutoff frequency of the low-pass filter.

The first parameter ω_4 can be easily achieved because the DG controller, VSC, and the feeder impedance are fixed in Tables I and II. The second design parameter ω_c is selected to be five times higher than the current loop bandwidth. Finally, K_s should be designed to ensure that the magnitude in the range of $[f_1, f_2]$ is within the stability region.

The green curve in Fig. 22 shows the bode plot of the stabilizing loop admittance $Y_s(s) = G_s(s)Y_g(s)/G_\tau(s)$, where $\omega_4 =$ 3070 rad/s, $\omega_c = 15\,000$ rad/s, and $K_s = 22$. Obviously, the phase of $G_s(s)Y_g(s)/G_\tau(s)$ has the same characteristics as $Y_g(s)/G_\tau(s)$ at a low-frequency bandwidth. Then, the impedance of $Y_s(s)$ can be completely corrected to positive damping characteristic above f_4. Meanwhile, the magnitude of $Y_s(s)$ is increased in the range of $[f_1, f_2]$ to be covered by the magnitude stability region. Fig. 23 further shows the control performance of active-damping control. By comparing $Z_i(s)$ and $Z_{is}(s)$, it is known that employing active-damping control method can suppress the phase advance of $Z_i(s)$ at the actual oscillation frequency to make the phase deviation between source-side impedance and load-side impedance meet the stability criterion, and thus improving the system stability margin.

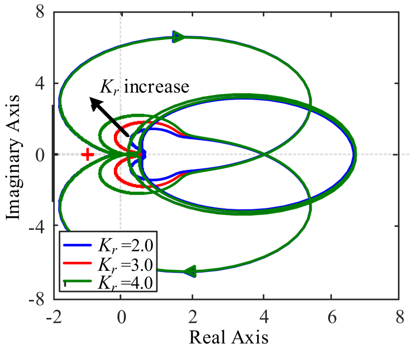

Fig. 24. Nyquist plots with different K_r when active-damping method is used.

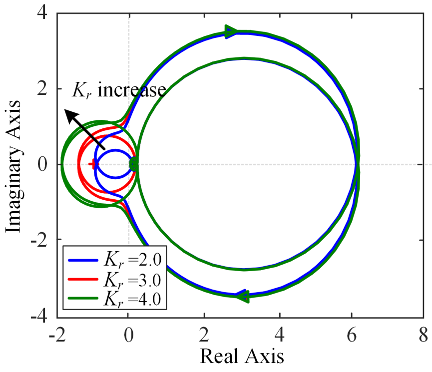

Fig. 25. Nyquist plots with different K_r when tradeoff method is used.

D. Performance Comparison Between IDS With Active-Damping Method and Tradeoff Method

The VPFOSF IDS with the tradeoff method [24] selects a conservative range of feedback gain K_r to ensure the enough stability margin. If the active-damping stabilizer is designed to suppress the phase advance issue caused by the increase of K_r, the grid-connected system stability margin can be improved while enhancing the islanding detection speed compared to the tradeoff method. To validate the superiority of the active-damping method, their stability margin variation with the K_r increasing is shown in Fig. 24. It clearly shows that the Nyquist contour of T(s) does not encircle $(-1, 0)$ with the K_r rising when using active-damping method, but the stability margin based on tradeoff method is deteriorated, as shown in Fig. 25. Moreover, with the transmission line length L increasing from 1 km to 6 km, the stability margin when using the active-damping stabilizing method is studied in Fig. 26. It can be seen that the stability margin is little affected compared with Fig. 15 because the phase advance issue has been suppressed. These results mean that the overall system based on the proposed active-damping method has a faster islanding detection capability while guaranteeing system stability under grid-connected conditions.

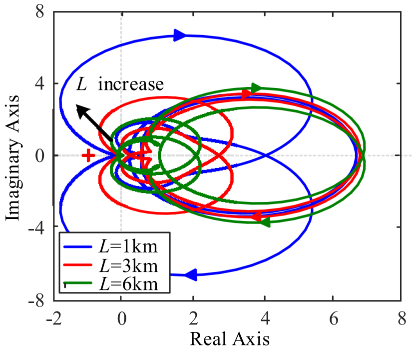

Fig. 26. Nyquist plots with different transmission line lengths when active-damping method is used.

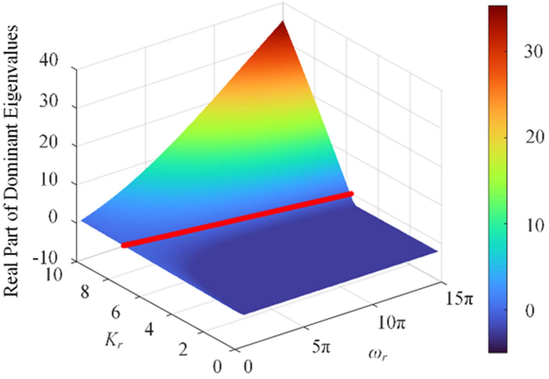

Fig. 27. Real part of dominant eigenvalues with different K_r and ω_r of grid-connected system using the active-damping method.

The compensation performance can be further analyzed by the characteristic equation of the grid-connected system. When the proposed active-damping method is used, the real part of dominant eigenvalues of grid-connected system with the value of K_r and ω_r increasing is displayed in Fig. 27.

Comparing Figs. 16 and 27, the value of K_r corresponding to the stability boundary in the gird-connected mode becomes much larger after using the proposed stabilizing control, allowing the system stability margin to be improved. Finally, according to Figs. 17 and 27, the effective design that makes the dc microgrid realize rapid islanding detection while guaranteeing stability in the grid-connected mode are depicted in Region I of Fig. 28. As long as ensuring the K_r staying in the Region I, the active-damping stabilizing loop can always remain active to effectively address the conflict between detection speed and system stability. Similarly, the effective combinations with the tradeoff method are located in Region II, which is fully covered by Region I. Comparing with the tradeoff method, using the active-damping method not only can achieve faster islanding detection in Region II, but also greatly improve the overall system stability margin, allowing the system keeps stable even outside the Region II.

V. SIMULATION RESULTS

In this section, the performance of the proposed active-damping scheme is evaluated in the grid-connected dc microgrid

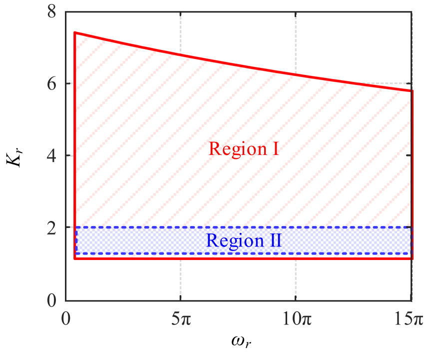

Fig. 28. Stability margin comparison between the proposed active-damping method and conventional tradeoff method.

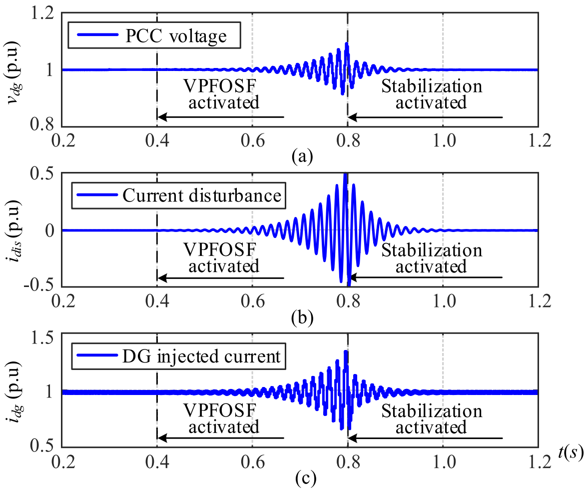

Fig. 29. System response at grid-connected operation.

shown in Fig. 1 under the MATLAB/Simulink environment. Then, the capability of islanding detection is assessed with both the VPFOSF IDS and the proposed stability enhancement method used. Furthermore, the system robustness is tested under different operating conditions. Also, the advantages of the proposed active-damping method are validated by comparing with the conventional methods. Finally, the operation performance of a two-DG system is assessed. The system simulation parameters are listed in Tables I and II.

A. Grid-Connected Test

The test is carried out to examine the grid-connected operation performance with the VPFOSF IDS. K_r and ω_r are set to 3 and 15 π, respectively. Fig. 29 shows the system responses with VPFOSF and proposed stabilizing control. First, the PCC voltage shown in Fig. 29(a) is driven to lose stability in the grid-connected mode when the VPFOSF loop is enabled at $t = 0.4$ s, which is in accordance with the stability analysis presented in Fig. 14. Meanwhile, the current disturbance excites mutually with the PCC voltage and causes the oscillation of DG injected current. Then, the proposed stabilizing scheme is activated at $t = 0.8$ s. Affected by the active-damping loop, the PCC voltage

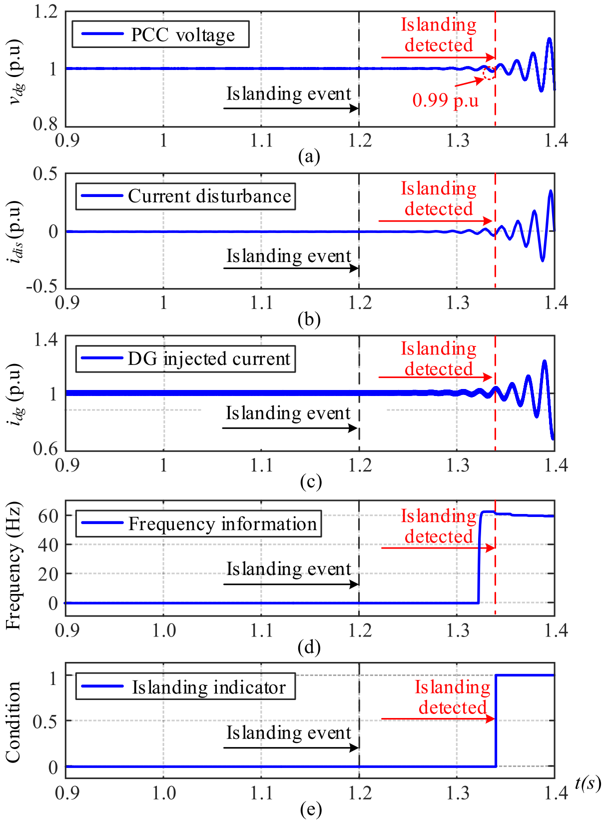

Fig. 30. System response after an islanding event.

and DG injected current are restored to 1.0 p.u. within 0.2 s, as depicted in Fig. 29(a) and (c). The well-damped performance proves the effectiveness of the proposed stabilizing control.

B. Islanding Test

Once the islanding event occurs, the VPFOSF scheme causes an oscillation with the selected frequency in the PCC voltage. On the other hand, the active-damping control is designed to mitigate the oscillation under grid-connected conditions. Thus, it is important to evaluate the islanding detection performance with both the VPFOSF and proposed stabilizing scheme used. In this study case, the DG and load operate at their rated power to satisfy power neutralizing, which is the worst condition to detect islanding events. The resonant frequency f_0 is selected to be 60 Hz, the positive feedback gain K_r is 3, and resonant bandwidth ω_r is set to 10 π. As shown in Fig. 30(a) and (b), the PCC voltage is stable in the grid-connected mode and the current disturbance is close to zero because of the stabilizing loop effect. At $t = 1.2$ s, the islanding event occurs, the PCC voltage is driven to oscillate at 60 Hz due to the loss of the voltage support, as shown in Fig. 30(a) and (d). Also, the disturbing current excites mutually with the PCC voltage and causes the oscillation of the DG injected current in the islanding mode, as indicated in Fig. 30(b) and (c). Finally, the islanding event can be detected within 0.14 s with less voltage fluctuation, which is only 0.01 p.u. Because of the good power quality, the control mode of DG can be transferred to the constant voltage control seamlessly after the islanding event is detected. As described in Fig. 31, the PCC voltage smoothly recovers to 1.0 p.u. after successful detection, which improves the power supply reliability during the islanding modes. This case indicates that the functionality of the proposed active-damping stabilizing method would not conflict with the VPFOSF IDS.

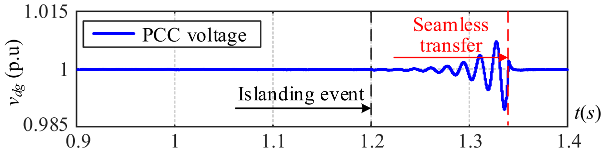

Fig. 31. Seamless transfer after an islanding event under resistive load condition.

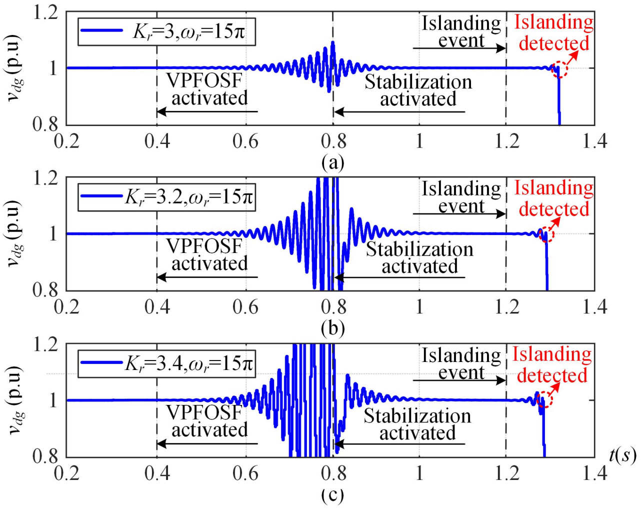

Fig. 32. Voltage response with K_r rising.

C. Parameter Validation Test

In this test, the positive feedback gain K_r is set as 3, 3.2, and 3.4, respectively, to examine the compensation performance of the proposed active-damping scheme. As depicted in Fig. 32, the oscillation magnitude of the PCC voltage becomes larger with the K_r increasing, but all of them can be suppressed within 0.2 s when stabilization is activated, which matches the stability analysis shown in Fig. 24. Moreover, the detecting time under three conditions decreases with the K_r rising and the DG stops supplying power to loads after islanding events are detected. This result shows that the proposed active-damping compensator may effectively address the conflict between islanding detection speed and grid-connected system stability.

D. Robustness Test

The system dynamic response in different operation conditions is tested to assess the robustness of the grid-connected system with the proposed stabilizing schemes. Then, the impact of load switching, DG power changing, and VSC voltage changing on the DG equipped with both the VPFOSF scheme and proposed stabilizing control is simulated, as shown in Fig. 33.

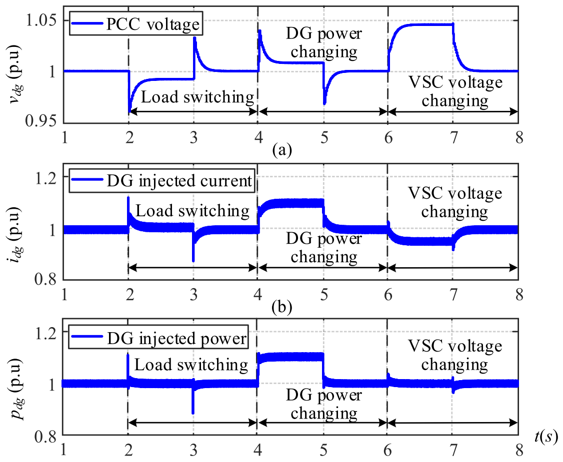

Fig. 33. Stabilized system response against perturbations caused by load switching, DG power changing and VSC voltage changing.

It is distinctly noticed that the active-damping control can preserve system stability effectively when the VPFOSF scheme is enabled. Furthermore, the pure resistive load increases by 0.1 p.u. at $t = 2$ s and decreases by 0.1 p.u. at $t = 3$ s. The DG injected power increases by 0.1 p.u. at $t = 4$ s and decreases by 0.1 p.u. at $t = 5$ s. These external large disturbances result in a voltage sudden change at DG PCC, and then the voltage regulation loop of the VSC works to regulate the bus voltage to enter a new steady state within 0.3 s, as shown in Fig. 33(a). Finally, the dc gird voltage changes by $+5\%$, -5% of rated voltage at 6 and 7 s, respectively. Although the response of PCC voltage is determined by the VSC control bandwidth without the sudden change, the total regulation time in these three operation cases is the same because the responses in the PCC voltage are all dominated by the voltage loop dynamics of the VSC. It is also noted that the DG injected current dynamics show negligible overshoots, and the DG injected power is nearly unchanged at the steady state, as presented in Fig. 33(b) and (c). These results indicate the good robustness of the proposed stabilizing control scheme.

Furthermore, CPL conditions and constant current load (CCL) conditions are considered for testing the islanding detection performance when DG is equipped with the proposed active-damping stabilizing scheme. The simulation results of DG PCC voltage under two different load conditions are displayed in Fig. 34. It clearly shows that the islanding event under both conditions can be detected within 2 s. The DG transfers seamlessly to the constant voltage control after successful islanding detection. It is also worth noting that the detection speed under both CPL conditions and CCL conditions are faster than that under pure resistive conditions shown in Fig. 31 as the resistive load has the largest NDZ. These cases indicate that the proposed IDS is applicable for any load conditions.

E. Comparison Test

To validate the advantages of the proposed control method in improving power quality, islanding detection speed, and grid-connected system stability, three cases are carried out using the proposed active-damping method, conventional FBPF method, and tradeoff method, respectively. In the first test case, the K_r and ω_r are selected to be 3 and 15 π, respectively, and the positive feedback gain of the FBPF method is set to 1.3. As shown in Fig. 35, the oscillation amplitude of the FBPF method is much higher than that of the VPFOSF after the islanding event occurring at 1.2 s. Then, the islanding condition is detected after 130 ms with a small voltage fluctuation of only 0.03 p.u. by VPFOSF method, while the FBPF method requires the PCC voltage to be shifted out of 0.88 p.u. to detect islanding events. It indicates the VPFOSF method has good power quality and faster detection speed. In the second test case, the oscillation frequency with the tradeoff method is set to 45 Hz [24]. K_r and ω_r are selected to be 1.8 and 15 π, respectively. Fig. 36(a) shows that both methods can keep stable during grid-connected modes and detect islanding events successfully utilizing the frequency information, but the detection speed based on the proposed active-damping method is faster than that based on the conventional tradeoff method. In the last test case, K_r and

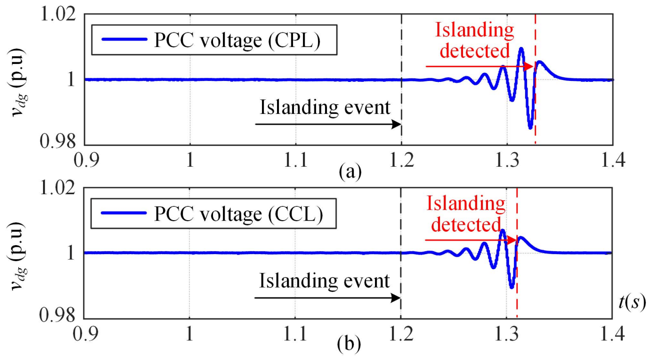

Fig. 34. Islanding detection performance under CPL and CCL conditions.

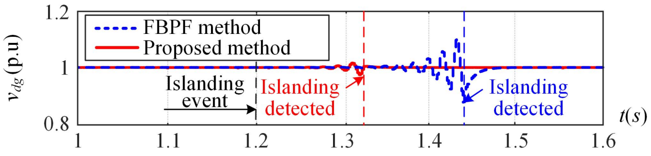

Fig. 35. Comparison of islanding detection performance when DG using FBPF method and proposed active-damping method.

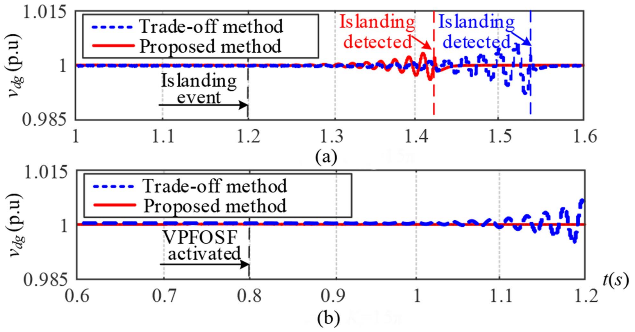

Fig. 36. Performance comparison under islanding and grid-connected station when DG using tradeoff method and proposed active-damping method.

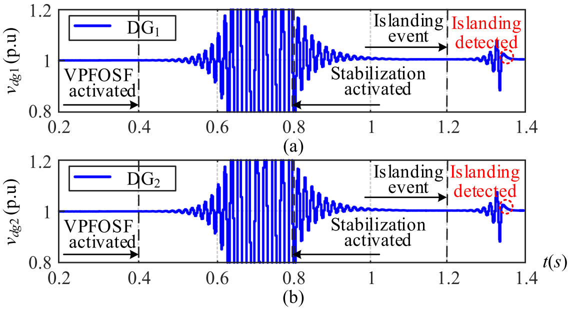

Fig. 37. System response of a two-DG system.

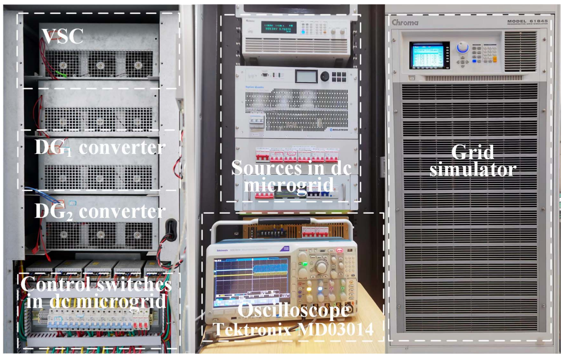

Fig. 38. Experimental setup of dc microgrid.

ω_r are set to 3 and 15 π, respectively. Fig. 36(b) shows that the DG equipped with the proposed active-damping method can still operate normally, but the system with tradeoff method loses stability in the grid-connected mode after VPFOSF IDS is activated. This result is completely consistent with the stability margin analysis given in Fig. 28. It concludes that the proposed stabilizing scheme is a more effective way to solve the conflict between islanding detection speed and grid-connected system stability.

F. Multiple DGs System Test

Moreover, the effectiveness of the proposed active-damping control has been also verified in the multiple-DG system. The simulation parameters of the two DGs are the same, where $K_r = 3$, $\omega_r = 15\pi$, and $f_0 = 60$ Hz. As shown in Fig. 37, the oscillation of PCC voltage is much more serious after the VPFOSF is activated than the signal-DG system as Fig. 29, but when the stabilizing control is enabled at 0.8 s, each DG can recover to the stable state within 0.2 s. Finally, after an islanding event occurs, successful islanding detection costs only 135 ms. These results further validate the effectiveness of the proposed stabilizing scheme.

VI. EXPERIMENTAL VALIDATION

To verify the theoretical analysis, a downscaled laboratory prototype is established with the parameters listed in Tables I and II, as presented in Fig. 38. A dc source and buck converter are used as a DG unit to support resistive loads. A Chroma 61800-series ac grid simulator and VSC are employed to regulate the dc bus voltage. A Tektronix MD03014 oscilloscope is used to record the experimental waveform, which can provide four digital channels, meeting the requirements of measuring multiple parameters.

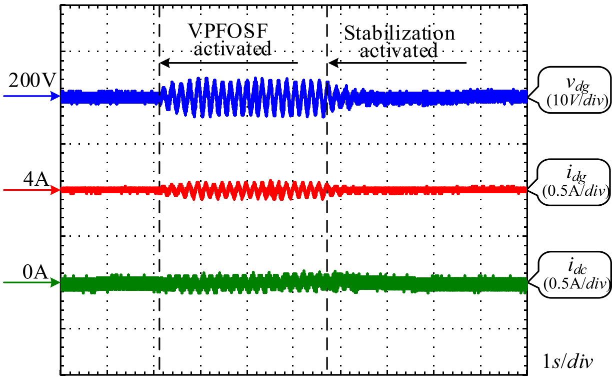

Fig. 39. System response at grid-connected operation.

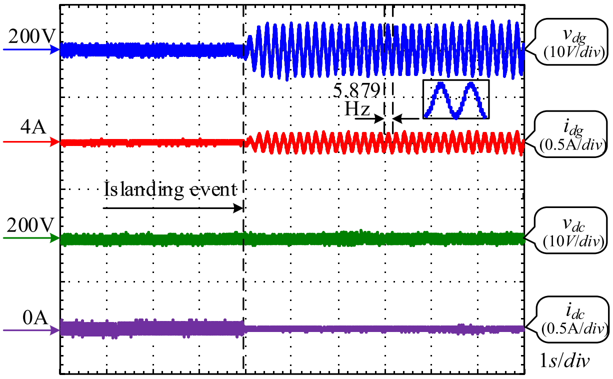

Fig. 40. System response after an islanding event in a single DG system.

A. Grid-Connected Test

The effect of employing the active-damping loop is first investigated in Fig. 39 for a grid-connected dc system with VPFOSF scheme. Obviously, the dc system is stable until the VPFOSF is enabled, where the K_r and ω_r are selected as 0.06 and 2 π, and oscillation frequency is selected as 6 Hz as it is the most sensitive frequency based on the analysis of the experiment parameters. Then, PCC voltage v_{dg}, DG injected current i_{dg}, and dc grid current i_{dc} begin to oscillate, as presented in Fig. 39. After the proposed stabilizing scheme is activated, the system gradually restores its stability, showing a well-damped performance.

B. Islanding Test

Then, the islanding test is carried out by setting the power of generation exactly neutralizes the power consumption to ensure the ability of the VPFOSF IDS under the worst scenario. The experimental results are depicted in Fig. 40. After an islanding event, the dc grid voltage v_{dc} keeps 200 V, while the dc grid current i_{dc} recovers to zero because of the disconnection between

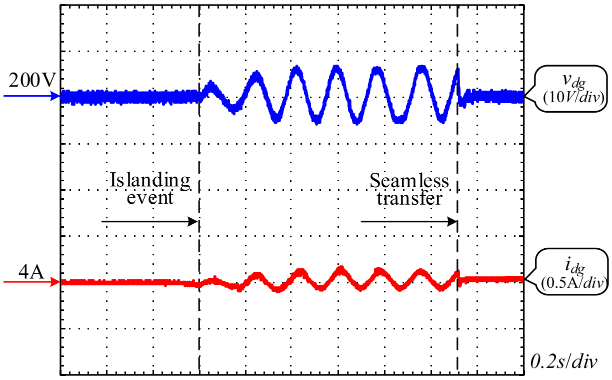

Fig. 41. Seamless transfer after an islanding event is detected.

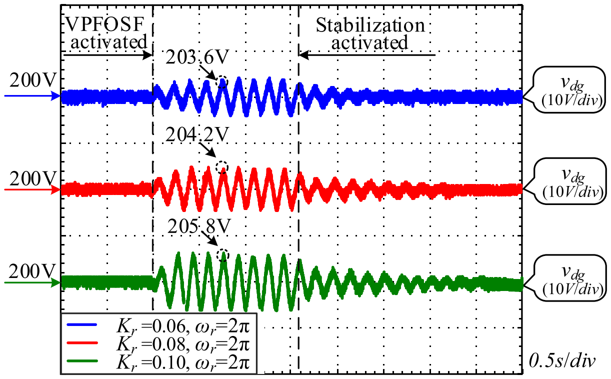

Fig. 42. Voltage responses with K_r increasing under grid-connected conditions.

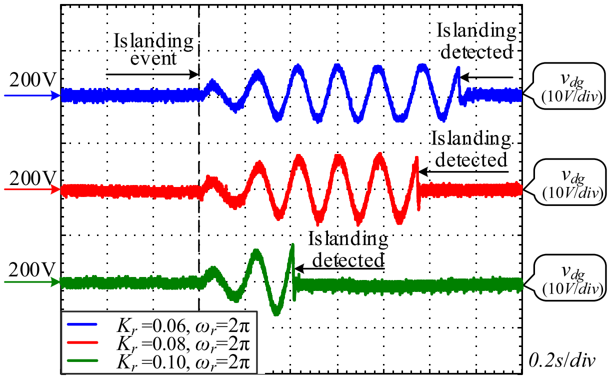

Fig. 43. Voltage responses with K_r increasing under islanding conditions.

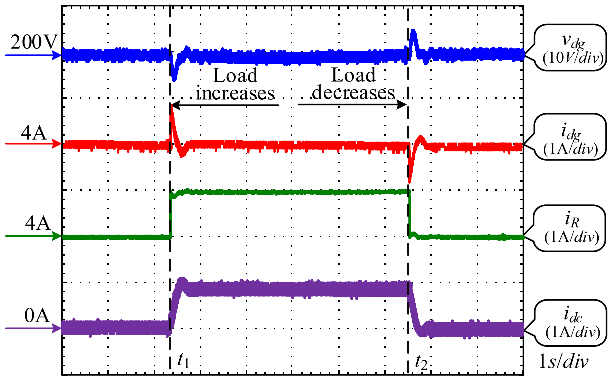

Fig. 44. System response with load switching at grid-connected operation.

the VSC and PCC. Besides, the PCC voltage $v_{\rm dg}$ and DG injected current $i_{\rm dg}$ gradually oscillate at the selected frequency after an islanding event. Fig. 40 shows the practical oscillation frequency of $v_{\rm dg}$ is 5.879 Hz, which corresponds with the theoretical selection (6 Hz). At the same time, the oscillation amplitude of PCC voltage is only 0.03 p.u., which shows the advantages of VPFOSF scheme in good power quality. After successful detection, the DG is switched to constant voltage control mode to ensure the islanding system reliability. The whole seamless transfer process is presented in Fig. 41.

C. Parameter Validation Test

Furthermore, the impacts of K_r variation on the grid-connected stability and islanding detection speed are shown in Figs. 42 and 43, respectively. Fig. 42 shows that the rising of K_r increases the oscillation amplitude of PCC voltage under grid-connected conditions, but all three cases can restore the system stability after the active-damping control is activated. These results demonstrate the universal validity of the proposed stability enhancement scheme. Moreover, Fig. 43 indicates that the islanding detecting time under three cases decreases with the K_r rising. After the islanding event is detected, the control target of DG is switched to the voltage regulation mode. By comparing the three different operation cases, it can be concluded that the proposed active-damping method effectively improves the DG islanding detection speed and grid-connected stability margin.

D. Robustness Test

To test the robustness of the grid-connected operation when both the VPFOSF IDS and active-damping control are used, the impact of switching load on the PCC voltage is evaluated, as shown in Fig. 44. The resistive load increases by 25% at t_1 and decreases by 25% at t_2. It shows that the maximum overshoot of the $v_{\rm dg}$ waveform is less than 5% during the transient periods. Meanwhile, the response of dc grid current $i_{\rm dc}$ indicates that the variation of load power is fully undertaken by the utility grid. These results prove the good robustness of the proposed stabilizing control.

E. Multiple DGs System Test

Finally, the operation performance of the proposed stability enhancement control in a two-DG system is examined. The experimental parameters are the same for both DGs, where K_r and ω_r are selected to be 0.06 and 2 π, respectively. Comparing with the single system response in Fig. 39, Fig. 45 shows that more severe instability condition in each DG is suppressed by the active-damping scheme, which agrees with the previous simulation results. Once the islanding event occurs, the voltage starts to oscillate at the selected frequency, and the DG system

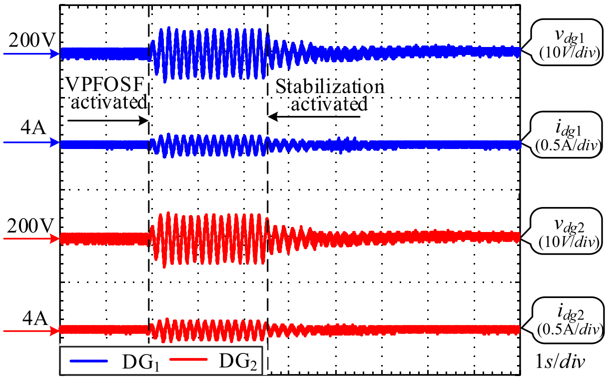

Fig. 45. System response under grid-connected conditions in two-DG system.

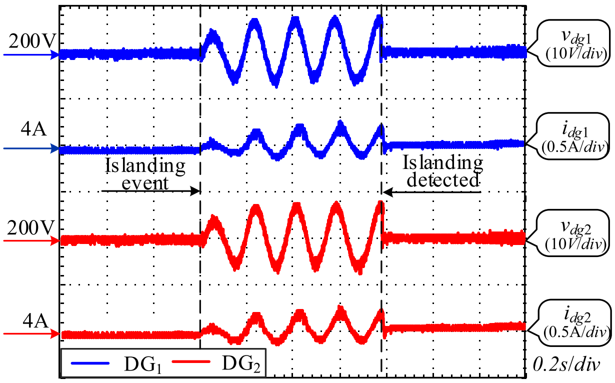

Fig. 46. System response under islanding conditions in two-DG system.

transfers to the constant voltage control after the islanding event is detected, as shown in Fig. 46. These results further validate the effectiveness of the proposed stability enhancement scheme.

VII. CONCLUSION

In this article, an active-damping control scheme has been proposed to address the conflict among islanding detection speed, power quality, and grid-connected system stability. First, the detailed output impedance models of the VSC and DG equipped with VPFOSF IDS are developed and analyzed, which reveal the impact of VPFOSF loop on the system stability. With the positive feedback gain increasing, the islanding detection speed can be improved but the grid-connected system stability margin would be highly influenced. The root cause of this instability is that the phase deviation between source-side impedance and load-side impedance exceeds $-180°$ at the oscillation frequency caused by the VPFOSF loop. On the basis of this, the stability region has been investigated and described in detail to guide the design method of active-damping compensator, and a grid-current-based stabilizing loop is developed in the DG controller to suppress the phase advance of load-side impedance and therefore the overall system stability margin is effectively improved. In this manner, the rapid islanding detection and good power quality can be realized, and grid-connected system stability is also ensured. Finally, the theoretical analysis and results have been validated by both detailed full-scale simulation and laboratory-scale experiments.

REFERENCES

[1] T. Dragičević, X. Lu, J. C. V. Asquez, and J. M. Guerrero, “DC microgrids—Part I: A review of control strategies and stabilizing techniques,” *IEEE Trans. Power Electron.*, vol. 31, no. 7, pp. 4876–4891, Jul. 2016.

[2] W. Xie, M. Han, W. Cao, J. M. Guerrero, and J. C. Vasquez, “System-level large-signal stability analysis of droop-controlled DC microgrids,” *IEEE Trans. Power Electron.*, vol. 36, no. 4, pp. 4224–4236, Apr. 2021.

[3] J. Zeng, Q. Wang, J. Liu, J. Chen, and H. Chen, “A potential game approach to distributed operational optimization for microgrid energy management with renewable energy and demand response,” *IEEE Trans. Ind. Electron.*, vol. 66, no. 6, pp. 4479–4489, Jun. 2019.

[4] V. A. Kleftakis, D. T. Lagos, C. N. Papadimitriou, and N. D. Hatziargyriou, “Seamless transition between interconnected and islanded operation of dc microgrids,” *IEEE Trans. Smart Grid*, vol. 10, no. 1, pp. 248–256, Jan. 2019.

[5] N. Vafamand, M. H. Khooban, T. Dragičević, F. Blaabjerg, and J. Boudjadar, “Robust non-fragile fuzzy control of uncertain dc microgrids feeding constant power loads,” *IEEE Trans. Power Electron.*, vol. 34, no. 11, pp. 11300–11308, Nov. 2019.

[6] Y. C. Jeung, D. C. Lee, T. Dragičević, and F. Blaabjerg, “Design of passivity-based damping controller for suppressing power oscillations in DC microgrids,” *IEEE Trans. Power Electron.*, vol. 36, no. 4, pp. 4016–4028, Apr. 2021.

[7] P. Wang, X. Lu, X. Yang, W. Wang, and D. G. Xu, “An improved distributed secondary control method for DC microgrids with enhanced dynamic current sharing performance,” *IEEE Trans. Power Electron.*, vol. 31, no. 9, pp. 6658–6673, Sep. 2016.

[8] D.-H. Dam and H.-H. Lee, “A power distributed control method for proportional load power sharing and bus voltage restoration in a DC microgrid,” *IEEE Trans. Ind. Appl.*, vol. 54, no. 4, pp. 3616–3625, Aug. 2018.

[9] L. Herrera, W. Zhang, and J. Wang, “Stability analysis and controller design of DC microgrids with constant power loads,” *IEEE Trans. Smart Grid*, vol. 8, no. 2, pp. 881–888, Mar. 2017.

[10] L. Zhou et al., “Virtual positive-damping reshaped impedance stability control method for the offshore MVDC system,” *IEEE Trans. Power Electron.*, vol. 34, no. 5, pp. 4951–4966, May 2019.

[11] H. Vahedi, R. Noroozian, A. Jalilvand, and G. B. Gharehpetian, “A new method for islanding detection of inverter-based distributed generation using DC-link voltage control,” *IEEE Trans. Power Del.*, vol. 26, no. 2, pp. 1176–1186, Apr. 2011.

[12] “*IEEE Standard for Interconnection and Interoperability of Distributed Energy Resources With Associated Electric Power Systems Interfaces*,” IEEE Std. 1547, 2018.

[13] C. Li, C. Cao, Y. Cao, Y. Kuang, L. Zeng, and B. Fang, “A review of islanding detection methods for microgrid,” *Renewable Sustain. Energy Rev.*, vol. 35, pp. 211–220, Apr. 2014.

[14] H. R. Baghaee, D. Mlakić, S. Nikolovski, and T. Dragičević, “Antiislanding protection of PV-based microgrids consisting of PHEVs using SVMs,” *IEEE Trans. Smart Grid*, vol. 11, no. 1, pp. 483–500, Jan. 2020.

[15] H. R. Baghaee, D. Mlakić, S. Nikolovski, and T. Dragičević, “Support vector machine-based islanding and grid fault detection in active distribution networks,” *IEEE J. Emerg. Sel. Topics Power Electron.*, vol. 8, no. 3, pp. 2385–2403, Sep. 2020.

[16] A. Makkieh et al., “Assessment of passive islanding detection methods for DC microgrids,” in *Proc. 15th IET Int. Conf. AC DC Power Transmiss.*, 2019, pp. 1–6.

[17] C. N. Papadimitriou, V. A. Kleftakis, and N. D. Hatziargyriou, “A novel method for islanding detection in dc networks,” *IEEE Trans. Sustain. Energy*, vol. 8, no. 1, pp. 441–448, Jan. 2017.

[18] B. K. Choudhury and P. Jena, “Superimposed impedance-based passive islanding detection scheme for DC microgrids,” *IEEE J. Emerg. Sel. Topics Power Electron.*, vol. 10, no. 1, pp. 469–483, Feb. 2022.

[19] F. Paz and M. Ordonez, “An impedance-based islanding detection method for dc grids,” in *Proc. 9th IEEE Int. Symp. Power Electron. Distrib. Gener. Syst.*, 2018, pp. 1–7.

[20] K. Jia, Z. Zhu, Q. Zhao, Z. Yang, and T. Bi, “Islanding detection method of multi-port photovoltaic DC microgrid based on harmonic impedance measurement,” *IET Renewable Power Gener.*, vol. 13, no. 14, pp. 2604–2611, Oct. 2019.

[21] H. Chen et al., “An impedance-based islanding detection method for DC microgrid with multiple distributed generators,” *CSEE J. Power Energy Syst.*, to be published, doi: 10.17775/CSEEJPES.2022.00020.

[22] G. S. Seo, K. C. Lee, and B. H. Cho, “A new DC anti-islanding technique of electrolytic capacitor-less photovoltaic interface in DC microgrids,” *IEEE Trans. Power Electron.*, vol. 28, no. 4, pp. 1632–1641, Apr. 2013.

[23] A. M. I. Mohamad and Y. A. R. I. Mohamed, “Assessment and performance comparison of positive feedback islanding detection methods in DC microgrids,” *IEEE Trans. Power Electron.*, vol. 32, no. 8, pp. 6577–6594, Aug. 2017.

[24] Q. Huang, H. Chen, X. Xiang, C. Li, W. Li, and X. He, “Islanding detection with positive feedback of selected frequency for DC microgrid systems,” *IEEE Trans. Power Electron.*, vol. 36, no. 10, pp. 11800–11817, Oct. 2021.

[25] A. M. I. Mohamad and Y. A. I. Mohamed, “Analysis and mitigation of interaction dynamics in active DC microgrids with positive feedback islanding detection schemes,” *IEEE Trans. Power Electron.*, vol. 33, no. 3, pp. 2751–2773, Mar. 2018.

[26] A. M. I. Mohamad and Y. A. I. Mohamed, “Impedance-based analysis and stabilizing of active DC microgrids with positive feedback islanding detection schemes,” *IEEE Trans. Power Electron.*, vol. 33, no. 11, pp. 9902–9922, Mar. 2018.

[27] Y. Gu, X. Xiang, W. Li, and X. He, “Mode-adaptive decentralized control for renewable DC microgrid with enhanced reliability and flexibility,” *IEEE Trans. Power Electron.*, vol. 29, no. 9, pp. 5072–5080, Sep. 2014.

[28] L. Xu and D. Chen, “Control and operation of a DC microgrid with variable generation and energy storage,” *IEEE Trans. Power Del.*, vol. 26, no. 4, pp. 2513–2522, Oct. 2011.

[29] K. Ogata, *Modern Control Engineering*, 5th ed. Englewood Cliffs, NJ, USA: Prentice-Hall, 2010.

[30] R. Middlebrook, “Input filter considerations in design and application of switching regulators,” in *Proc. IEEE Ind. Appl. Soc. Annu. Meeting*, 1976, pp. 366–382.

[31] J. Sun, “Impedance-based stability criterion for grid-connected inverters,” *IEEE Trans. Power Electron.*, vol. 26, no. 11, pp. 3075–3078, Nov. 2011.

[32] J. Lei, Z. Qin, W. Li, P. Bauer, and X. He, “Stability region exploring of shunt active power filters based on output admittance modeling,” *IEEE Trans. Ind. Electron.*, vol. 68, no. 12, pp. 11696–11706, Dec. 2021.

[33] X. Huang et al., “Stability assessment and coordinated impedance shaping strategy for DC bidirectional cascaded system with LC input filter,” *Int. J. Elect. Power Energy Syst.*, vol. 115, 2020, Art. no. 105429.

[34] Y. Xia, M. Yu, X. Wang, and W. Wei, “Describing function method based power oscillation analysis of LCL-filtered single-stage PV generators connected to weak grid,” *IEEE Trans. Power Electron.*, vol. 34, no. 9, pp. 8724–8738, Sep. 2019.

[35] Y. Xia, W. Wei, M. Yu, and P. Wang, “Stability analysis of PV generators with consideration of P&O-based power control,” *IEEE Trans. Ind. Electron.*, vol. 66, no. 8, pp. 6483–6492, Aug. 2019.

[36] Z. Chen, X. Huang, A. Lou, J. Yang, and L. Yang, “Wideband harmonic resonance characteristics and coordinated damping method for distributed generation power plant,” *IEEE Trans. Ind. Electron.*, vol. 66, no. 10, pp. 7753–7764, Oct. 2019.

[37] W.-J. Lee and S.-K. Sul, “DC-link voltage stabilizing for reduced DC-link capacitor inverter,” *IEEE Trans. Ind. Appl.*, vol. 50, no. 1, pp. 404–414, Jan. 2014.

[38] A. M. I. Mohamad and Y. A. R. I. Mohamed, “Investigation and enhancement of stability in grid-connected active dc distribution systems with high penetration level of dynamic loads,” *IEEE Trans. Power Electron.*, vol. 34, no. 9, pp. 9170–9190, Sep. 2019.

Tianling Shi (Student Member, IEEE) received the B.Sc. degree in electrical engineering and automation from the School of Electrical and Information Engineering, Jiangsu University, Zhenjiang, China, in 2018. He is currently working toward the Ph.D. degree in electrical engineering with the School of Mechatronic Engineering and Automation, Shanghai University, Shanghai, China.

His research interests include the control and protection of dc microgrids.

Hongyi Chen received the B.Sc. degree in electrical engineering from the North China Electric Power University, Beijing, China, in 2019. She is currently working toward the Ph.D. degree in electrical engineering with the College of Electrical Engineering, Zhejiang University, Hangzhou, China.

Her research interests include the control and protection of dc microgrids.

Boxin Liu received the B.Sc. degree in electrical engineering and automation from the School of Electrical Engineering and Automation, Hefei University of technology, Hefei, China, in 2020. He is currently working toward the Ph.D. degree in electrical engineering with the College of Electrical Engineering, Zhejiang University, Zhejiang, China.

His research interests include the analysis and control of grid-connected power electronic converters.

Shiyuan Fan received the B.Sc. degree in electrical engineering and automation from the North China Electric Power University, Beijing, China, in 2018. She is currently working toward the Ph.D. degree in electrical engineering with the Zhejiang University, Zhejiang, China.

Her research interests include topology, modulation, and control of modular multilevel converters.

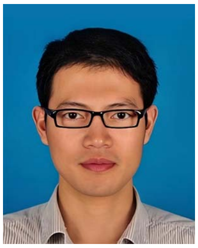

Fei Wang (Senior Member, IEEE) received the B.Sc. degree in electrical engineering and the M.Sc. degree in power electronics from the Zhejiang University, Hangzhou, China, in 2002 and 2005, respectively, and the Ph.D. degree in power electronics from the Eindhoven University of Technology, Eindhoven, The Netherlands, in 2010.

He was with the Philips Lighting Electronics Global Development Center, Shanghai, China, from 2005 to 2006. He has been a Faculty Member with the School of Mechatronic Engineering and Automation, Shanghai University, Shanghai, China, since 2010, and became a Professor in March 2018. He has authored/coauthored more than 100 technical papers, 1 academic book, and also 10 authorized invention patents. His research interests include distributed generation, electrical drives, power quality, LED drivers, and smart grid.

Xin Xiang (Senior Member, IEEE) received the B.Sc. degree from the Harbin Institute of Technology, Harbin, China, in 2011, the M.Sc. degree from the Zhejiang University, Hangzhou, China, in 2014, and the Ph.D. degree from the Imperial College London, London, U.K., in 2018, all in electrical and electronic engineering.

From 2018 to 2020, he was a Research Associate with the Imperial College London. He is currently a tenure-track Associate Professor with the College of Electrical Engineering, Zhejiang University, Hangzhou, China. His research interests include the analysis and control of power electronics converters for power system applications.

Dr. Xiang was the recipient of the Eryl Cadwaladr Davies Prize for the Best Ph.D. Thesis of Electrical and Electronic Engineering Department, Imperial College London, and the Best Ph.D. Thesis Award from IEEE PELS U.K. and Ireland Chapter.

Huan Yang (Member, IEEE) received the B.Sc. and Ph.D. degrees in electrical engineering & its automation and electrical engineering from the Zhejiang University, Hangzhou, China, in 2003 and 2008, respectively.

From January 2009 to March 2011, he was a Postdoctoral Fellow with the Zhejiang University. In March 2011, he became a Faculty Member with the Zhejiang University, as a Research Associate. In December 2012, he became an Associate Professor of electrical engineering with the Zhejiang University. From April 2012 to April 2013, he conducted joint research with the Fuji Electric Co., Ltd., Tokyo, Japan, as the Oversea Researcher of New Energy and Industrial Technology Development Organization. He has authored/coauthored more than 50 papers and holds more than 10 issued/pending patents. His research interests include distribution generation and microgrids, high-performance motor systems, and smart power distribution equipment.

Wuhua Li (Member, IEEE) received the B.Sc. and Ph.D. degrees in power electronics and electrical engineering from the Zhejiang University, Hangzhou, China, in 2002 and 2008, respectively.

From 2004 to 2005, he was a Research Intern, and from 2007 to 2008, a Research Assistant with the GE Global Research Center, Shanghai, China. From 2008 to 2010, he joined the College of Electrical Engineering, Zhejiang University, as a Postdoctor. In 2010, he was promoted as an Associate Professor. Since 2013, he has been a Full Professor with the Zhejiang University. From 2010 to 2011, he was a Postdoctoral Fellow with the Department of Electrical and Computer Engineering, Ryerson University, Toronto, ON, Canada. He is currently the Executive Deputy Director of the National Specialty Laboratory for Power Electronics and the Vice Director of the Power Electronics Research Institute, Zhejiang University. He has authored/coauthored more than 300 peer-reviewed technical papers and holds more than 50 issued/pending patents. His research interests include power devices, converter topologies, and advanced controls for high-power energy conversion systems.

Prof. Li was the recipient of the 2012 Delta Young Scholar from Delta Environmental & Educational Foundation, 2012 Outstanding Young Scholar from National Science Foundation of China, 2013 Chief Youth Scientist of National 973 Program, 2014 Young Top-Notch Scholar of National Ten Thousand Talent Program, and 2019 Distinguished Young Scholar from National Science Foundation of China, due to his excellent teaching and research contributions. He serves as the Associated Editor of *Journal of Emerging and Selected Topics in Power Electronics*, *IET Power Electronics*, *CSEE Journal of Power and Energy Systems*, *CPSS Transactions on Power Electronics and Applications*, and *Proceedings of the Chinese Society for Electrical Engineering*, Guest Editor of *IET Renewable Power Generation* for Special Issue “DC and HVDC system technologies,” and Member of Editorial Board for *Journal of Modern Power System and Clean Energy*. He was the recipient of one National Natural Science Award and four Scientific and Technological Achievement Awards from the Zhejiang Provincial Government and the State Educational Ministry of China. He has been appointed as the most cited Chinese Researchers by Elsevier, since 2014.